

Extended Gas in Seyfert Galaxies: Near-Infrared Observations of 15 Active Nuclei

Cláudia Winge^{1,★†}, Thaisa Storchi-Bergmann^{1,★}, Martin J. Ward^{2,★}
and Andrew S. Wilson^{3,4,★}

¹ *Instituto de Física, UFRGS, Av. Bento Gonçalves, 9500, C.P. 15051. CEP 91501-970, Porto Alegre, RS, Brazil.*

² *Dept. of Physics and Astronomy, University of Leicester, University Road, Leicester LE1 7RH, England*

³ *Astronomy Program, University of Maryland, College Park, MD 20742, USA*

⁴ *Space Telescope Science Institute, 3700 San Martin Dr., Baltimore, MD 21218, USA*

Accepted December 8, 1999; Received August 24, 1999

ABSTRACT

Results from an analysis of low resolution ($R \sim 250$) near-IR long-slit spectra covering simultaneously the I, J, H, and K bands, for a sample of 15 Seyfert galaxies and the NGC 5253 starburst nucleus, are presented. The Seyfert galaxies were selected as presenting ‘linear’ or cone-like high excitation emission line in the optical, most probably due to the collimation of the central source’s radiation by a dusty molecular torus. Our goal was to look for signatures of this torus, and to investigate the gaseous distribution, excitation and reddening. The strongest emission lines detected are usually He I $1.083\mu\text{m}$ and [S III] $\lambda 9532$, followed by Pa β . In some cases, [Fe II] $1.26\mu\text{m}$ and $1.64\mu\text{m}$ are also seen. [Fe II] $1.26\mu\text{m}$ and H₂ $\nu=1-0$ S(1) are detected in some of the higher resolution spectra obtained for five galaxies. The emission lines are spatially extended in most cases, and we have used the [Fe II]/Pa β ratio as a measure of the gaseous excitation in Mrk 573, NGC 1386, and NGC 7582. Values for this ratio between 1.5 and 6 are found, suggesting excitation of [Fe II] by X-rays or shock waves in some regions. Broad permitted lines are observed in three Seyfert 1 galaxies. Nuclear Pa β in NGC 1365, and possibly nuclear Br γ in Mrk 573, are also broad.

From analysis of the spatial distribution of the continuum ($J-H$) and ($H-K$) colours derived from our spectra, we find redder colours for the nucleus than the nearby bulge in most of the Seyfert 2s observed. Comparison with models including emission from dust and stars shows that hot ($T \sim 1000$ K) dust emission dominates the nuclear continuum in NGC 1365, NGC 2110, NGC 3281, NGC 7582, and ESO362-G18. In NGC 1386, NGC 5643, and NGC 5728 the main contributor is the underlying stellar population, combined with some foreground reddening and/or cooler dust emission. In a few cases, the ($J-H$) colours on opposite sides of the nucleus differ by 0.3 – 0.8 mag, an effect that we interpret as partly due to differences in the local stellar population, and possibly extinction gradients.

Key words:

1 INTRODUCTION

In the unified model for active galactic nuclei (AGN) the nuclear engine is surrounded by an optically thick, dusty toroidal structure, which collimates the escaping photons and, at the same time, hides the true nucleus from our line

of sight (Antonucci 1993). Observational evidence for such a model come from optical spectropolarimetry, which reveals that a number of Seyferts 2s show broad emission lines and blue continuum in polarized light (Miller & Goodrich 1990; Tran 1995), and emission-line imaging, which shows elongated morphologies for the extended emission line regions, with striking conical or bi-conical structures that can be traced down to a few tens of parsecs from the nucleus and which are generally aligned with the radio ejecta (Pogge 1989; Storchi-Bergmann & Bonatto 1991; Wilson & Tsvetanov 1994).

* Visiting Astronomer at the Cerro Tololo Interamerican Observatory, operated by the Association of Universities for Research in Astronomy, Inc. under contract with the National Science Foundation

† CNPq Fellowship

There are few observational constraints on the geometry of the torus, although red features and dust lanes (e.g., Wilson et al. 1993; Simpson et al. 1996b) aligned perpendicular to the radio/extended line emission axis are seen in some high resolution images. Hot dust ($T \sim 1200$ K) has been found to be an important contributor to the near-infrared nuclear continuum of Seyfert galaxies (Glass & Moorwood 1985; Kotilainen et al. 1992; Alonso-Herrero et al. 1998). Theoretical models (Krolik & Begelman 1988) show that for the dust to reach this temperature, the inner edges of the torus must be only a few parsecs from the nuclear source. The total extent of the torus, however, is not well constrained, and may reach several tens or even a hundred parsecs. Warm dust ($T \approx 600 - 800$ K) is presumably responsible for the observed mid-infrared flux (Pier & Krolik 1993).

Infrared spectroscopy of a number of Seyfert 2 galaxies has revealed broad components in the hydrogen emission-lines (e.g., Veilleux, Goodrich & Hill 1997 and references therein), thus confirming, at least in those particular cases, the presence of an obscured broad-line region. The torus is expected to contain warm molecular hydrogen, whose vibration-rotational transitions, especially $H_2 \nu=1-0$ S(1), could be used as a tracer of the size and geometry of the toroidal structure (Blietz et al. 1994; Moorwood et al. 1996; Marco, Alloin & Beuzit 1997). On the other hand, while the H_2 emission is expected to be extended perpendicular to the collimation/radio emission axis, emission lines from ionized gas (such as $[Fe II] 1.26\mu m$) should be emitted preferentially along the collimation axis, either due to photoionization by the hard photons from the central source or by shocks from the interaction of the radio jet with the ambient gas.

To address these issues, we obtained long-slit spectra in the near-infrared I, J, H, and K bands of a sample of Seyfert galaxies with known elongated or bi-conical high-excitation optical emission, which, in the unified model, is a direct result of the presence of the collimating torus. We also observed NGC 5253, a classical H II galaxy. Our first results, on NGC 2110 and the Circinus galaxy, have already been published (Storchi-Bergmann et al. 1999, hereafter Paper I), and in this paper we present the data for the remaining galaxies observed.

2 DATA REDUCTION

Long-slit spectra of the sample galaxies were obtained using the Infrared Spectrograph (IRS) on the 4m ‘Blanco’ telescope of the Cerro Tololo Interamerican Observatory in October-November, 1995 and February-March, 1996. The detector used was a 256×256 InSb device, with a $0''.363$ per pixel scale. The useful slit length was about $15''$, and the slit width was either $1''$ or $1''.7$, depending on the seeing, which was generally between these two values. The majority of the spectra were obtained using a low-resolution ($R \sim 250$), cross-dispersed grating (hereafter, the XD grating), which splits the complete $0.9 - 2.3 \mu m$ spectra into four or five segments, roughly coincident with the R, I, J, H, and K spectral bands. A few galaxies were also observed using either a 75 lines per mm grating, with resolution $R \sim 700$ (4 pixels), hereafter the LR grating, or a 210 lines per mm grating, $R \sim 2000$, hereafter the HR grating.

The log of observations is listed in Table 1. We observed most of the galaxies with the slit aligned along the position angle (PA) of the major axis of the inner isophotes in narrow-band ($[O III]$) images or along the radio axis (identified by an ‘r’ in Column 3). In a few cases, spectra were also obtained along the perpendicular direction (‘p’) or, for the Seyfert 1 objects, along arbitrary PAs. For NGC 5253 the slit was positioned along the major axis of the $H\alpha$ emission structure in the inner $\sim 25''$. Further details of the individual spectra are given in Section 3. To obtain the linear spatial scales in Table 1, we adopted $H_0 = 75 \text{ km s}^{-1} \text{ Mpc}^{-1}$.

Both XD and LR/HR data were reduced using IRAF[‡] scripts kindly provided by R. Elston at CTIO (available at the CTIO ftp archive), and followed standard procedures. The reduction of the LR and HR data has already been described in Paper I. The only difference here is that, after bias subtraction, flatfielding, and sky subtraction, removal of the atmospheric absorption features and flux calibration were performed on the full frame, instead of on the extracted spectra.

For the XD data, the fundamental difference from the standard IR data reduction is the tracing of the distortion across the slit (the wavelength direction). This was done using the spectrum of a bright star or pinhole, which was traced in each ‘band’ with a 4th order Legendre polynomial in the `aptrace` task. Similarly, the flat-fields were created using `apnormalize` rather than `response`, and then the individual segments of each image (corresponding approximately to the five colour bands) were flat-fielded, and ‘straightened’ using the solution previously found with the tracing star/pinhole spectrum. Wavelength calibration was performed using an HeAr lamp, with different solutions for each ‘band’. Low (2 – 4) order Legendre polynomials were fitted to a sample of 4 (K) to 12 (R) lines, resulting in the spectral intervals, pixel scales, and rms residuals of the fits listed in Table 2. Atmospheric absorption correction and flux calibration followed the same procedures as for the LR/HR data.

3 RESULTS

The integrated spectra of the sample galaxies, corresponding to the co-added emission within a $7 - 8''$ spatial window are shown in Figures 1a to 1e for the XD data. For the LR/HR data, the extraction windows were as listed on Table 4 and the resulting integrated spectra are shown in Figures 2a and 2b. Inside the atmospheric absorption bands, the XD data was masked out when the signal was below 10 percent of the peak transmission in the uncalibrated frames. The main emission lines are indicated, and total line fluxes are listed in Tables 3 and 4. In the XD sub-sample, the strongest lines are the $He I + Pa\gamma$ blend and $[S III] \lambda 9532$ emission. The uncertainties in the integrated fluxes are dominated by the continuum placement, and we estimate them to be of the

[‡] IRAF is distributed by the National Optical Astronomy Observatories, which are operated by the Association of Universities for Research in Astronomy, Inc., under cooperative agreement with the National Science Foundation.

Table 1. Log of Observations

Object	Date	P.A. ($^{\circ}$)	Grating/Band	Exp. Time (sec)	Slit width ($''$)	Spatial scale (pc/ $''$)
NGC 526A	1995 Oct 30	123	XD	1100	1.1	373
NGC 1097	1995 Oct 31	77	LR J	1200	1.1	82
NGC 1365	1995 Oct 30	130	XD	600	1.1	106
	1995 Oct 31	145	LR J	2400	1.1	
NGC 1386	1996 Feb 28	0	XD	800	1.1	56
NGC 2110	1996 Feb 28	350 (r)	XD	800	1.1	148
NGC 3281	1996 Feb 28	45	XD	800	1.1	224
NGC 4388 ^a	1996 Feb 27	13	XD	1200	1.1	78
	1996 Feb 27	90 (p)	XD	800	1.1	
	1996 Feb 29	13	HR J	2200	1.7	
	1996 Feb 29	90 (p)	HR J	2200	1.7	
NGC 5253	1996 Feb 28	43	XD	400	1.1	26
NGC 5643	1996 Feb 28	90	XD	800	1.1	78
NGC 5728	1996 Feb 28	20 (p)	XD	400	1.1	180
	1996 Feb 28	110	XD	800	1.1	
NGC 7582	1995 Oct 30	203	XD	900	1.1	102
IC 5063 ^b	1995 Nov 01	90	LR K	2520	1.1	220
ESO 362-G18	1995 Oct 30	68 (p)	XD	900	1.1	245
Fairall 9	1995 Oct 30	123	XD	600	1.1	911
Mrk 509	1995 Oct 30	0	XD	600	1.1	667
Mrk 573	1995 Oct 31	125 (r)	LR J	3000	1.1	335
	1995 Nov 01	35 (p)	LR K	3240	1.1	

^a Bad seeing ($\sim 2''.5$) for the HR spectra at PA=13 $^{\circ}$.

^b Clouds.

Table 2. Cross-dispersed Grating Wavelength Calibrations

Run	Band	Range (μm)	Pixel (\AA)	rms (\AA)
1995 Oct 30	I	0.802 – 1.195	16	2
	J	0.961 – 1.435	19	7
	H	1.199 – 1.792	23	10
	K	1.601 – 2.364	30	32
1996 Feb 27	I	0.865 – 1.260	16	3
	J	1.038 – 1.513	19	3
	H	1.296 – 1.890	24	7
1996 Feb 28	K	1.602 – 2.691	43	66
	R	0.772 – 0.999	13	26
	I	0.851 – 1.226	16	2
	J	0.972 – 1.447	19	5
	H	1.213 – 1.806	24	4
	K	1.616 – 2.404	31	16

order 20 – 25% for the XD spectra, and 10 – 20% for the LR/HR data.

Table 5 lists the full width at half maximum (FWHM), corrected for instrumental resolution, of the lines observed at different positions for the four objects with HR/LR spectra. The errors are due to the uncertainty in the placement of the continuum and represent maximum values. Due to its higher S/N ratio, the emission lines in a spectrum of the planetary nebula NGC 7009 were used as the reference (instrumental) profile for the LR grating. These values were found to be in very good agreement with the FWHM of the sky lines. For the HR grating the instrumental profile was given by the HeAr calibration lamp lines.

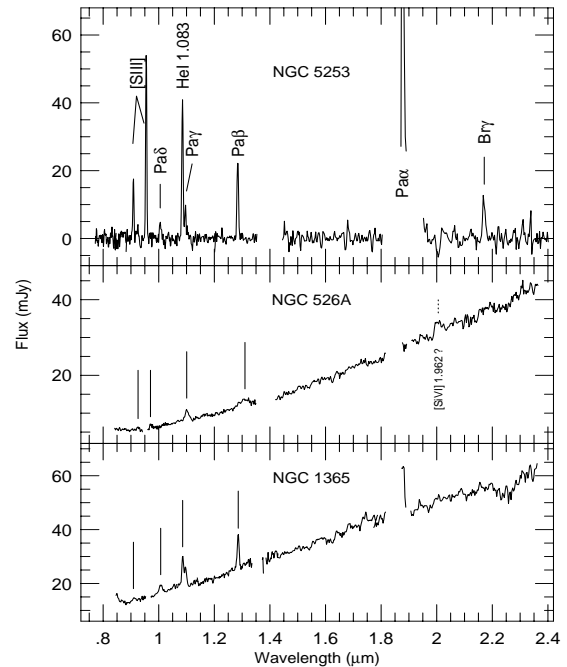


Figure 1. (a) Integrated spectra of the galaxies observed with the XD grating. NGC 5253, NGC 526A, and NGC 1365

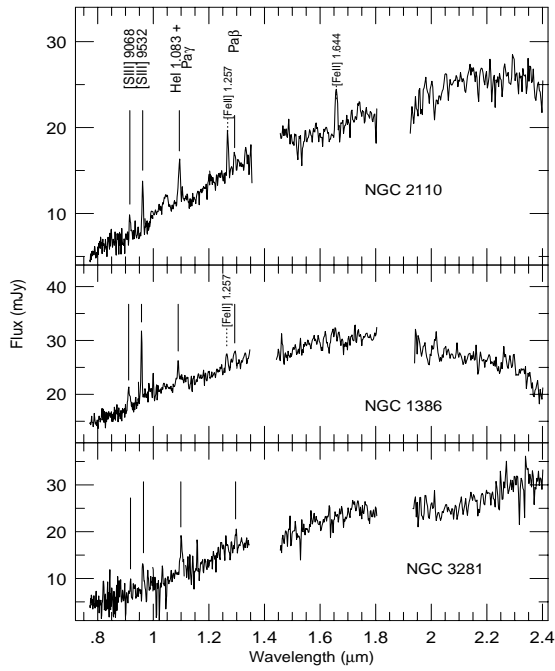


Figure 1 – *continued* (b) NGC 2110, NGC 1386, and NGC 3281

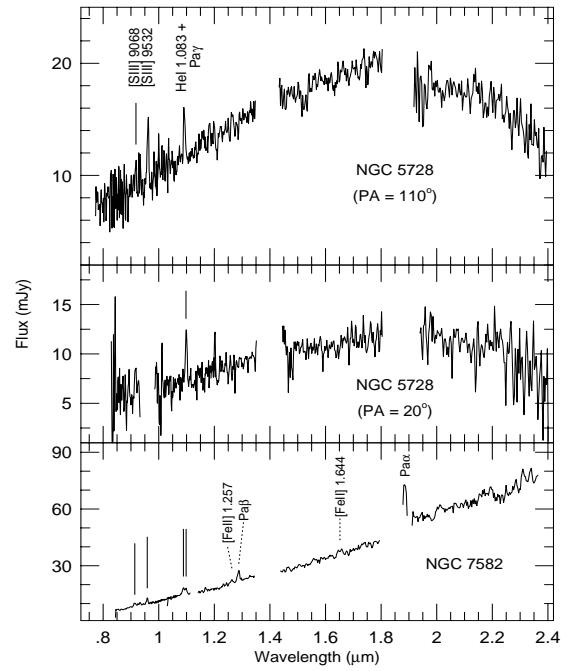


Figure 1 – *continued* (d) NGC 5728 (PA=110° and 20°), and NGC 7582

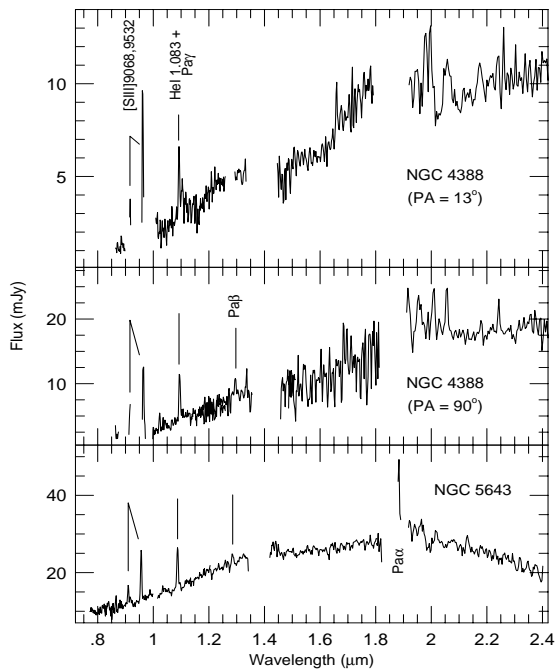


Figure 1 – *continued* (c) NGC 4388 (PA=13° and 90°), and NGC 5643

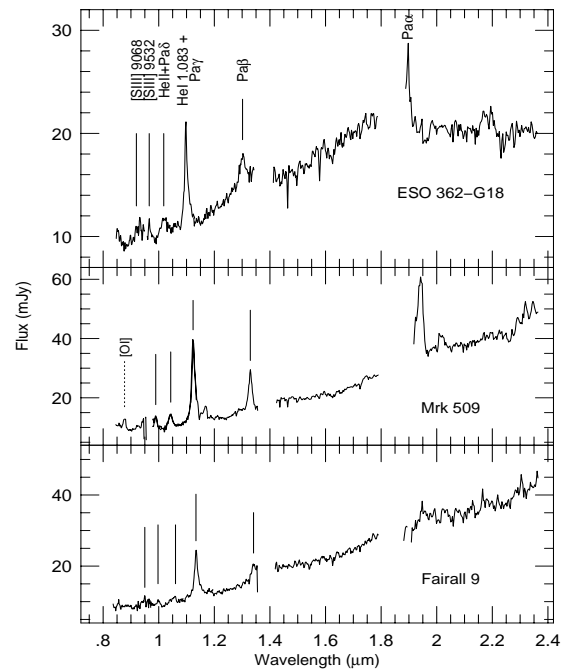
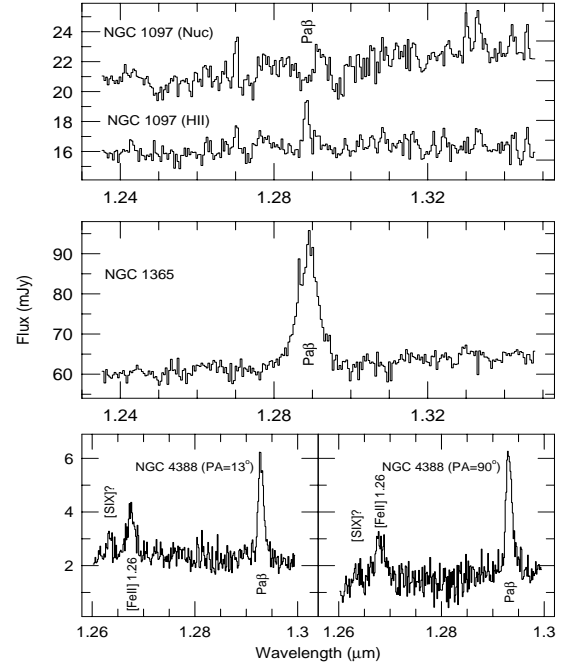


Figure 1 – *continued* (e) ESO 362-G18, Mrk 509, and Fairall 9

Table 3. Integrated line fluxes from the spectra obtained with the XD grating (in units of 10^{-14} ergs cm $^{-2}$ s $^{-1}$).

Object	Line ID	Flux
NGC 526A	[S III] 9532	3.9
	He I+Pa γ	11.7
	Pa β	11.5
NGC 1365	[S III] 9532	11.5
	Pa δ	3.1
	He I 1.083	26.6
	Pa γ	14.7
NGC 1386	[S III] 9068	6.5
	[S III] 9532	16.1
	He I+Pa γ	6.6
NGC 2110	[Fe II] 1.26	5.3
	Pa β	3.5
	[S III] 9068	4.9
	[S III] 9532	11.8
NGC 3281	He I+Pa γ	10.1
	[Fe II] 1.26	7.0
	Pa β	3.4
	[Fe II] 1.64	6.2
NGC 4388 (PA=13)	[S III] 9068	7.6
	[S III] 9532	24.1
NGC 4388 (PA=90)	He I+Pa γ	7.9
	[S III] 9532	8.4
NGC 5253	He I+Pa γ	5.7
	[S III] 9532	23.1
	Pa β	11.8
NGC 5643	Pa β	5.6
	Pa α	121.7
	Br γ	9.1
	[S III] 9068	8.7
	[S III] 9532	23.3
	He I+Pa γ	17.3
	Pa β	3.5
NGC 5728 (PA=110)	[S III] 9532	14.4
	He I+Pa γ	9.2
NGC 5728 (PA=20)	[S III] 9532	11.9
	He I+Pa γ	10.2
NGC 7582	[S III] 9532	5.7
	He I+Pa γ	14.7
	[Fe II] 1.26	2.1
	Pa β	7.8
ESO 362-G18	[Fe II] 1.64	5.0
	He I+Pa γ	35.0
	Pa β	10.1
Fairall 9	Pa α	>10.7
	[S III] 9532	9.0
	He II+Pa δ	7.7
	He I+Pa γ	51.5
Mrk 509	Pa β	15.3
	Pa α	>18.1
	[S III] 9532	13.3
	He II+Pa δ	21.9
	He I+Pa γ	108.0
	Pa β	33.0
	Pa α	>59.1


Figure 2. Integrated spectra of the sample galaxies observed with the LR/HR gratings (a) NGC 1097 – LR/J, NGC 1365 – LR/J, and NGC 4388 – HR/J (PA = 13° and 90°). The right hand scale on the top panel is the flux scale for the HII region spectrum in NGC 1097.

3.1 Extended Emission and Line ratios

Due to the low spectral resolution of the XD spectra, we opted to extract the emission line spatial distributions directly from the two-dimensional frames, rather than extracting a number of spectra along the slit and measuring the individual line fluxes as done in Paper I. The spatial profiles were obtained by extracting and co-adding all columns inside a spectral window wide enough to contain all the line emission, and the underlying continuum subtracted by linear interpolation between two windows at each side of the emission line. The errors were estimated by creating an image with the same ratio of the rms to the total raw counts (\sqrt{N}/N) in each pixel on the uncalibrated frames, then processing those images with the same procedure as used for the actual data.

With the exception of NGC 5253, where the geometric centre of the slit was arbitrarily set as the origin of the spatial axis, the centroid of a nearby continuum spatial profile was used as the origin of the emission line spatial distributions. No correction for foreground (Galactic) reddening was applied.

In most XD spectra, the emission lines with enough S/N ratio to allow the construction of meaningful spatial profiles were [S III] λ 9532, the He I+Pa γ blend and Pa β . The available emission lines allowed the determination of the internal reddening only in the H II galaxy NGC 5253, where we found average reddening corrected values of 3.1 and 4.7 for

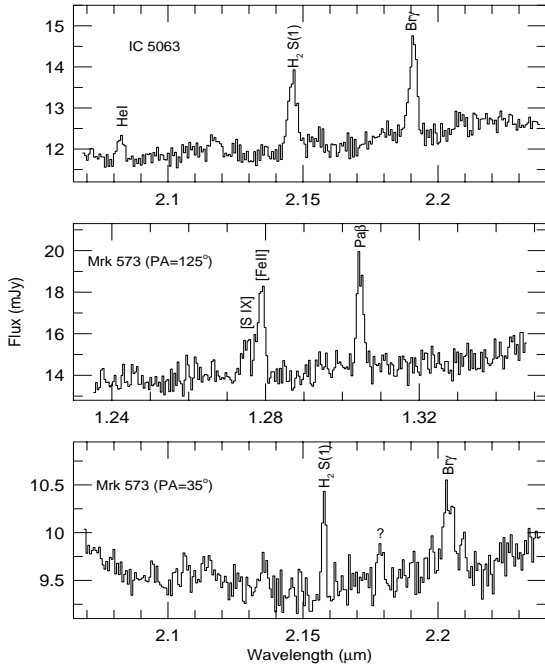


Figure 2 – *continued* (b) IC 5063 – LR/K, Mrk 573 – LR/J (PA = 125°), and Mrk 573 – LR/K (PA = 35°)

Table 4. Integrated line fluxes from the spectra taken with the LR/HR gratings (in units of 10^{-14} ergs cm^{-2} s^{-1})

Object	Window (")	Line ID	Flux
NGC 1365	10.96	Pa β (broad)	20.8
		Pa β (total)	41.3
NGC 4388 (PA=13)	3.65	[S IX]	2.2
		[Fe II] 1.26	6.7
NGC 4388 (PA=90)	4.38	Pa β	10.0
		[Fe II] 1.26	8.9
IC 5063	5.12	Pa β	12.2
		H ₂ S(1)	0.55
Mrk 573 (PA=125)	8.05	Br γ	0.45
		[S IX]	0.89
Mrk 573 (PA=35)	5.12	[Fe II] 1.26	1.89
		Pa β	2.03
Mrk 573 (PA=35)	5.12	H ₂ S(1)	0.14
		Br γ	0.37

The two entries for Pa β in NGC 1365 correspond to the fluxes in the broad component only (FWHM ≈ 1500 km s^{-1} ; see Table 5) and in all the emission line, respectively.

(He I+Pa γ)/Pa β , and [S III] $\lambda 9532$ /Pa β ratios, respectively. For the other galaxies, a good determination of the narrow emission line reddening could not be obtained, and any comparison among the resulting line ratios should be considered with caution. Some regularity was observed between the Seyfert 1 galaxies, which presented integrated line ratios (He I+Pa γ)/Pa $\beta \approx 3.4$, and [S III] $\lambda 9532$ /Pa $\beta \approx 0.4$. For the

Table 5. Intrinsic line widths (km s^{-1}). The upper block are measurements with the LR grating, the lower with the HR grating.

Object	Position (")	Line	FWHM
NGC 1365	Nuc	Pa β (N)	< 450
		Pa β (B)	1397 $^{+30}_{-15}$
		Pa β (VB)	2868 $^{+349}_{-729}$
IC 5063	4.02 NW	Pa β	159 $^{+48}_{-52}$
	4.02 SE	Pa β	210 $^{+53}_{-69}$
	Nuc	Br γ	< 400
	1.46 NW	H ₂ S(1)	< 400
Mrk 573 J	Nuc	Br γ	< 400
		H ₂ (S1)	483 $^{+82}_{-73}$
		[S IX]	< 450
Mrk 573 J	1.46 NW	[Fe II] 1.26 μm	323 $^{+54}_{-46}$
		Pa β	< 450
	1.46 SE	[Fe II] 1.26 μm	< 450
		Pa β	182 $^{+127}_{-102}$
Mrk 573 K	3.29 NW	Pa β	323 $^{+43}_{-127}$
		Pa β	< 450
	Nuc	Pa β	< 450
		Br γ	589 $^{+256}_{-135}$
NGC 7009	(instrumental, LR)	H ₂ S(1)	< 400
		Pa β	455 $^{+8}_{-13}$
		Br γ	403 $^{+10}_{-8}$
NGC 4388 (PA=13)	Nuc	[Fe II] 1.26 μm	297 $^{+32}_{-30}$
		Pa β	299 $^{+69}_{-24}$
NGC 4388 (PA=90)	Nuc	Pa β	378 $^{+62}_{-40}$
		1.46 W	Pa β
HeAr	(instrumental, HR)		148 \pm 1

Seyfert 2 nuclei, these same ratios span the ranges $1.0 \lesssim (\text{He I}+\text{Pa}\gamma)/\text{Pa}\beta \lesssim 4.9$ and $0.6 \lesssim [\text{S III}] \lambda 9532/\text{Pa}\beta \lesssim 6.7$.

We now describe the spatial distribution of the emission lines for each galaxy, comparing the light profiles in the emission lines with that of a reference star, and also the spatial variations in the available line ratios. For reasons of clarity in the figures, the emission line spatial profiles shown below have been rebinned to $0''.74$ per pixel.

NGC 5253: The spectrum of this H II galaxy (Figure 1a, top panel) was obtained along the PA of the major axis of the H α emission structure seen in Fig. 1a of Calzetti et al. (1997), with essentially no stellar continuum detected. The strong emission lines (Fig. 3) extend over $\sim 10''$ and peak at the central clump, corresponding to the starburst nucleus. To investigate their variation with distance from the nucleus, we constructed several line ratios. The [S III] $\lambda 9532/(\text{He I}+\text{Pa}\gamma)$ ratio varies from ~ 1.2 at $3''$ SW to ~ 2.8 at $3''$ NE, while the [S II] $\lambda 9532/\text{Pa}\beta$ is almost flat in the above interval, 2.78 ± 0.96 , rising slightly to the SW. The average reddening in the region $-3'' < r < 4''.5$, calculated from the Br $\gamma/\text{Pa}\beta$ ratio, assuming a case B intrinsic value of 0.171 (Osterbrock 1989), is $E(B-V) \sim 0.91 \pm 0.15$. However, large variations (as much as ~ 3 mag in $E(B-V)$) are found within a few pixels, in agreement with the work of Calzetti et al (1997), which detected a much higher reddening inside the emission clumps than indicated by the emission line ratios in the integrated optical spectrum. The (He I+Pa γ)/Pa β ratio, which can be interpreted

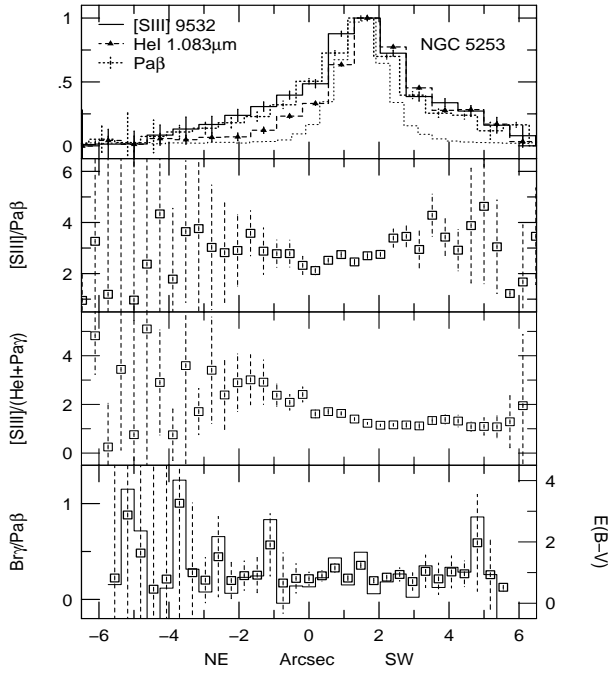


Figure 3. Normalized spatial distributions and line ratios of the main emission lines from the XD spectrum of NGC 5253. The dotted line in the upper panel is the spatial profile of the atmospheric standard star used in the data reduction and approximately represents the seeing profile. The full line in the bottom panel represents the value of $E(B-V)$ (right axis scale) calculated from the $Br\gamma/Pa\beta$ ratio (squares, left axis scale).

as a tracer of the ionization structure, varies from ~ 2 in the extended regions to up to 5.4 in the starburst nucleus. Assuming a case B recombination, and $A_V = 3 - 6$ mag, the contribution of $Pa\gamma$ to the blend varies between 0.45 to 0.36 the $Pa\beta$ flux. For the above range of reddening, the observed line ratios translate to $2.6 \lesssim He\,I\,1.083\mu m/Pa\beta \lesssim 3.5$, $1.9 \lesssim [S\,III]\,\lambda 9532/He\,I\,1.083\mu m \lesssim 2.2$ (both ratios corrected for the $Pa\gamma$ contribution), $4.7 \lesssim [S\,III]\,\lambda 9532/Pa\beta \lesssim 7.8$. The upper limits are consistent with H II regions models (Lumsden & Puxley 1996).

NGC 526A: The XD spectrum (Fig. 1a, middle) was obtained along the PA of the major axis of the [O III] emission (Mulchaey, Wilson & Tsvetanov 1996), and presents a steep continuum with faint emission lines. We detected the He I+Pa γ blend, Pa β , and a feature at $\sim 1.96\mu m$ which we tentatively identify as [Si VI] $1.962\mu m$. The lines are only barely spatially resolved (Fig. 4), with Pa β presenting some low surface brightness emission up to $\sim 4''$ SE. The $(He\,I+Pa\gamma)/Pa\beta$ ratio in the inner $4''$ ($|r| < 2''$) is 1.31 ± 0.13 .

NGC 1365: The XD spectrum (Fig. 1a, bottom), obtained along the axis of the ionization cone at PA = 130° , shows a red continuum, with prominent permitted lines (He II+Pa δ , He I+Pa γ , Pa β); Pa α is detected above the atmospheric absorption. The emission (Fig. 4) is resolved and similarly extended symmetrically from the nucleus in all lines, with the exception of a feature in

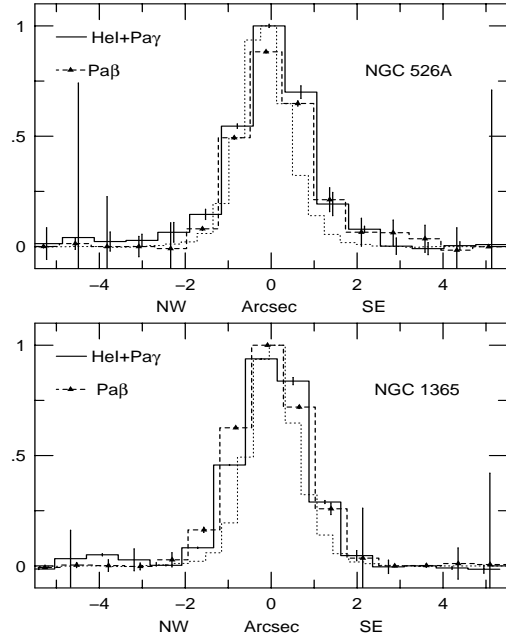


Figure 4. Spatial profiles of the main emission lines from the XD spectrum of NGC 526A (top) and NGC 1365 (bottom). As for NGC 5253, the dotted line is the stellar profile.

He I+Pa γ at $\sim 4''$ NW (the ‘anti-cone’ direction) which can be associated with an optical hot-spot in the circumnuclear star-forming ring (Storchi-Bergmann & Bonatto 1991; Kristen et al. 1997). The line ratios $(He\,I+Pa\gamma)/Pa\beta$ and $(He\,II+Pa\delta)/(He\,I+Pa\gamma)$ are essentially constant in the inner $4''$, with values 2.27 ± 0.12 and 0.19 ± 0.02 , respectively.

This galaxy was also observed with the LR grating in the J band. The spectrum (Fig. 2a, middle) shows very clearly the presence of a broad component in the nuclear Pa β profile (Fig. 5). The FWHM of the nuclear and extranuclear profiles, obtained using multiple Gaussian component decomposition, is listed in Table 5 for this and the other galaxies observed with the LR and HR gratings. At $4''$ NW and SE, Pa β is barely resolved spectrally (see Table 5).

The nuclear Pa β profile can be described as the sum of a narrow (N), broad (B) and very broad (VB) Gaussian components, with FWHM from 400 km s^{-1} to 2900 km s^{-1} . Véron et al. (1980) measured a flux of $7.7 \times 10^{-14}\text{ ergs cm}^{-2}\text{ s}^{-1}$ in their broad (FWHM $\sim 1300\text{ km s}^{-1}$) component of H α . Associating this emission system with the FWHM $\sim 1500\text{ km s}^{-1}$ component of Pa β observed here, we obtain a broad line region reddening of $A_V \sim 7.7$ mag for an intrinsic Pa $\beta/H\alpha$ ratio of 0.053. Since the broad lines of this galaxy are known to be variable (Giannuzzo & Stirpe 1996), not to mention calibration differences, this value is to be regarded as only a first order approximation to the actual broad-line region reddening.

Recently, Stevens, Forbes & Norris (1999) suggested that the optical broad lines in the nucleus of NGC 1365 could originate not at the Seyfert nucleus, but at one of the circumnuclear radio ‘hot spots’ (Morganti et al. 1999),

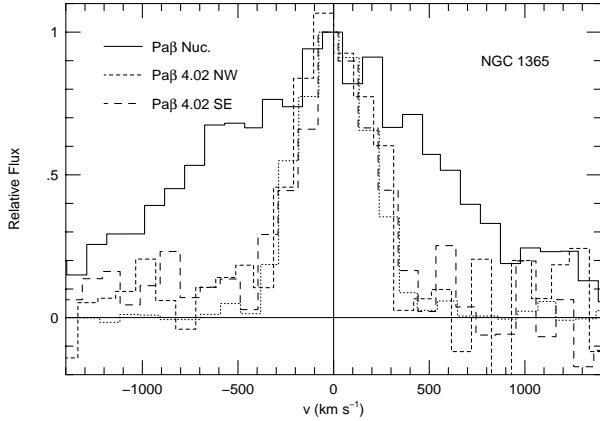


Figure 5. Comparison of the LR $\text{Pa}\beta$ spectral profiles of NGC 1365: nucleus (full line), $4''.02$ NW (short dash), and $4''.02$ SE (long dash). The dotted line is the $\text{Pa}\beta$ profile of NGC 7009, which is taken as representative of the instrumental resolution.

located at $\sim 5''$ SW of the optical nucleus, as a result of a radio-supernova located there. However, we find this highly unlikely, since our spectrum, which was obtained with a $1''$ slit, centred in the optical nucleus, and oriented at almost right angles with the PA of the hot spot in question, would not have included any of its emission.

NGC 1386: The XD spectrum (Fig. 1b, middle) was obtained along the direction of the high excitation optical emission line protrusion detected in the images of Storchi-Bergmann et al. (1996). The brightest line is $[\text{S III}] \lambda 9532$, with fainter $\text{He I} + \text{Pa}\gamma$, $[\text{Fe II}] 1.26\mu\text{m}$, and $\text{Pa}\beta$. Although noisy, the resulting spatial profiles are definitely extended along the $[\text{O III}]$ emission direction (Fig. 6). The $\text{He I} + \text{Pa}\gamma$ distribution is the most extended, reaching at least $4''.5$ N of the nucleus, the end of the slit. The $(\text{He I} + \text{Pa}\gamma)/\text{Pa}\beta$ ratio is 2.9 ± 1.0 in the inner $4''$. The $[\text{S III}] \lambda 9532$ and $[\text{Fe II}] 1.26\mu\text{m}$ spatial profiles are resolved but more concentrated, extending only up to $2''.5$. In the inner $4''$, the $[\text{S III}] \lambda 9532/(\text{He I} + \text{Pa}\gamma)$ ratio is essentially flat, with a value of 2.21 ± 0.21 , while $[\text{Fe II}] 1.26\mu\text{m}/\text{Pa}\beta$ increases from ~ 0.9 at $r = 2''$ S to ~ 6 at $2''$ N, with a value of ≈ 2 in the nucleus, indicating a higher excitation of the gas to the N, in agreement with the optical images.

Several mechanisms for the origin of $[\text{Fe II}]$ emission in Seyferts have been extensively discussed in previous works (Forbes & Ward 1993; Simpson et al. 1996a; Alonso-Herrero et al. 1997; Veilleux et al. 1997). In starbursts, if the mechanism generating the $[\text{Fe II}]$ emission is directly related to the one producing the radio emission in (radio) bright supernova remnants, Colina (1993) calculated that $[\text{Fe II}] 1.26/\text{Pa}\beta \leq 0.4$ is expected. The higher ratios observed in Seyferts would then indicate ionization by X-rays from the active nuclei or

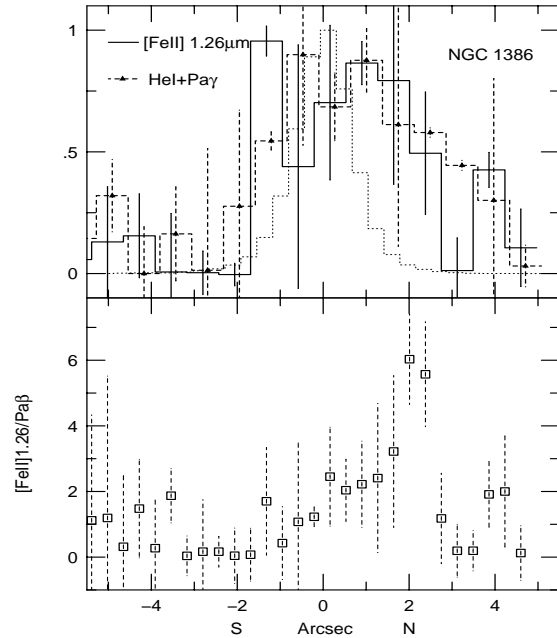


Figure 6. Spatial profiles and $[\text{Fe II}] 1.26\mu\text{m}/\text{Pa}\beta$ line ratio from the XD spectrum of NGC 1386. The dotted line is the stellar profile.

by shocks induced by the interaction of an outflow with the surrounding medium. However, if the lifetime of the $[\text{Fe II}]$ emission phase in single or multiple star formation bursts is longer than in Colina's models, the $[\text{Fe II}]/\text{Pa}\beta$ ratio can reach higher values (Vanzi, Alonso-Herrero & Rieke 1998), as the contribution from the remnants becomes dominant over the gas ionization from the aging H II regions.

Detailed stellar population analysis of NGC 1386 (Schmitt, Storchi-Bergmann & Cid Fernandes 1999) does not indicate the presence of a significant contribution from a young (10 Myr or less) component in the inner $2'' \times 2''$, and therefore the $[\text{Fe II}]/\text{Pa}\beta$ values indicate that, as is also found in NGC 2110 (Paper 1), a starburst related component of the $[\text{Fe II}]$ emission is not important in this case. Since this object was not observed with the higher resolution gratings, we do not have any information on the $[\text{Fe II}]$ line profile, but the line broadening in $\text{H}\alpha$ and $[\text{N II}] \lambda 6584$ within $1''.5$ N of the nucleus detected by Weaver, Wilson & Baldwin (1991) raises the possibility of shocks as an ionization source for the infrared $[\text{Fe II}]$ lines. Nagar et al. (1999) find the nuclear radio source to be extended by $0''.4$ in $\text{PA} = 170^\circ$, a similar direction to the extension of the optical emission lines.

NGC 2110: The HR/LR data for this galaxy were presented and analysed in Paper I, and we found evidence of shocks and X-rays as dominant sources of excitation for the $[\text{Fe II}]$ and H_2 emission in the inner few arcsec, respectively. The XD spectrum shown in Figure 1b (top panel) was obtained along the PA of the radio axis, with $[\text{S III}] \lambda 9068$, $[\text{S III}] \lambda 9532$, $\text{He I} + \text{Pa}\gamma$, $[\text{Fe II}] 1.26\mu\text{m}$, $\text{Pa}\beta$, and $[\text{Fe II}] 1.64\mu\text{m}$ detected. The spatial profiles of $[\text{S III}] \lambda 9532$, $\text{He I} + \text{Pa}\gamma$ and $\text{Pa}\beta$ are clearly asymmetric (Figure 7), be-

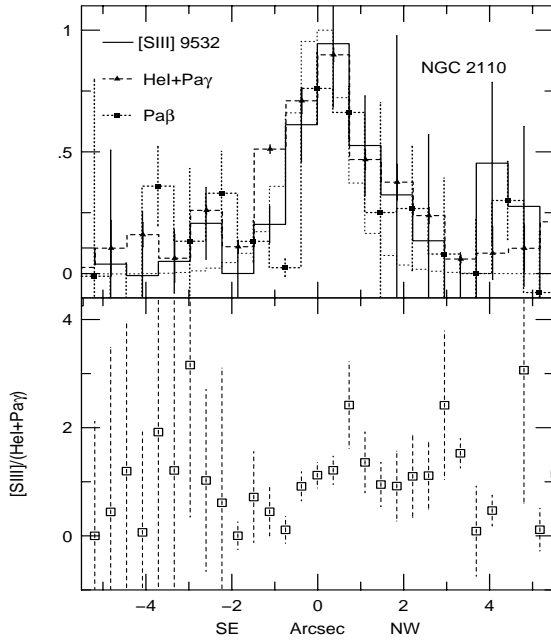


Figure 7. Spatial profiles and $[\text{S III}] \lambda 9532/\text{He I}+\text{Pa} \gamma$ line ratio from the XD spectrum of NGC 2110. The error bars in the $[\text{S III}] \lambda 9532$ profile have been excluded for clarity and are of similar amplitude to those in $\text{Pa} \beta$. The dotted line is the stellar profile.

ing extended up to $3''$ towards the NW, the direction of the high excitation optical emission. The $[\text{S III}]$ and $\text{Pa} \beta$ spatial profiles decline more quickly to the SE than the $\text{He I}+\text{Pa} \gamma$ profile, consistent with the isophotes in the $\text{H} \alpha + [\text{N II}]$ image of Mulchaey et al. (1996). The $[\text{Fe II}]$ spatial distribution (already discussed in Paper I) is similar to that of $[\text{S III}] \lambda 9532$. The $[\text{S III}] \lambda 9532/(\text{He I}+\text{Pa} \gamma)$ line ratio rises from 0.44 at $2''$ SE to 1.0 at $2''$ NW. A similar excitation gradient is seen in the $[\text{O III}] \lambda 5007/\text{H} \beta$ ratio (Wilson, Baldwin & Ulvestad 1985). The H_2 emission, clearly seen in the higher resolution spectra of Paper I, was not detected here because of the low resolution of the XD spectra.

NGC 3281: The XD spectrum is shown in Figure 1b (bottom panel). It shows only faint $[\text{S III}]$, He I , and $\text{Pa} \beta$ emission. The resulting spatial profiles were of too low S/N ratio to allow any useful analysis of the extended emission.

NGC 4388: Two sets of data were obtained for this object. The XD spectra (Fig. 1c, top and middle panels) were taken approximately along and perpendicular to the axis of the optical ionization cone, at $\text{PA}=13^\circ$ and 90° , respectively. The S/N is low, with only $[\text{S III}] \lambda 9532$ and $\text{He I}+\text{Pa} \gamma$ detected. The spatial profiles at $\text{PA} = 13^\circ$ (Fig. 8) are noisy, but more extended towards the NE, the anti-cone direction. The narrow-band $\text{H} \alpha + [\text{N II}]$ optical images of Veilleux et al. (1999) show an elongated structure in the inner $10''$, which also appears to be more extended to the NE direction (while the cone-like, kpc-scale high excitation gas distribution is oriented towards the south). Along $\text{PA}=90^\circ$ our emission line distributions are also resolved, but essentially symmetric with respect to the centre. The line ratios are almost

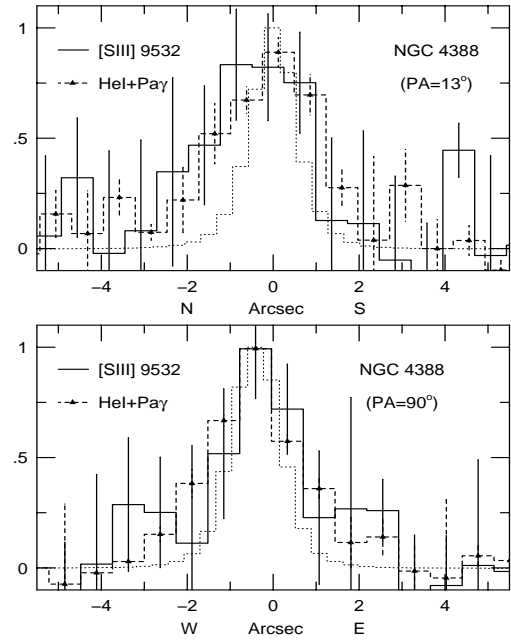


Figure 8. $[\text{S III}] \lambda 9532$ and $\text{He I}+\text{Pa} \gamma$ spatial profiles from the XD spectra of NGC 4388, at $\text{PA} = 13^\circ$ (top) and $\text{PA} = 90^\circ$ (bottom).

constant in the inner $4''$, with $[\text{S III}] \lambda 9532/(\text{He I}+\text{Pa} \gamma) = 1.58 \pm 0.84$ ($\text{PA}=13^\circ$) and 1.23 ± 0.74 ($\text{PA}=90^\circ$). In this latter spectrum, we also measured $[\text{S III}] \lambda 9532/\text{Pa} \beta \sim 4.30 \pm 0.50$ for this same region.

Two HR spectra in the J band were obtained at the same position angles as above (Figure 2a, bottom). The emission-lines spatial profiles are only marginally resolved at both PAs, with $[\text{Fe II}] 1.26 \mu\text{m}/\text{Pa} \beta \sim 0.7$. Along the cone direction, we clearly detect $[\text{S IX}] 1.262 \mu\text{m}$.

For the $\text{PA} = 90^\circ$ spectrum, the IRS imaging mode was used to find the position of the nucleus in the K band, which was found to be located $\sim 1''$ N of the optical position. The slit was thus centred offset by this amount from the optical nucleus. However, the continuum is a factor of two lower than that of the $\text{PA} = 13^\circ$ spectrum, and the $[\text{S IX}]$ line is not as clearly detected, suggesting that the true K-band nucleus was missed. The spatial offset between the optical and infrared nuclei in NGC 4388 has been previously noted by Stone, Wilson & Ward (1988), who found that the $10 \mu\text{m}$ emission peaks 'several arcsec' north of the optical nucleus, rising the possibility of the mid-infrared source to be associated with the radio ejecta, rather than with the nucleus proper.

The nuclear line profiles of $\text{Pa} \beta$ and $[\text{Fe II}] 1.26 \mu\text{m}$ from the $\text{PA}=13^\circ$ spectrum are spectrally resolved, and very similar to each other (Fig. 9). Correcting the observed widths in Table 5 by the instrumental broadening (adopted as the FWHM of $\text{Pa} \beta$ in NGC 7009) gives an intrinsic FWHM of $\sim 300 \text{ km s}^{-1}$ for both lines. Along the perpendicular direction ($\text{PA} = 90^\circ$), the nuclear $\text{Pa} \beta$ profile is resolved and marginally broader than at $\text{PA}=13^\circ$, with a corrected

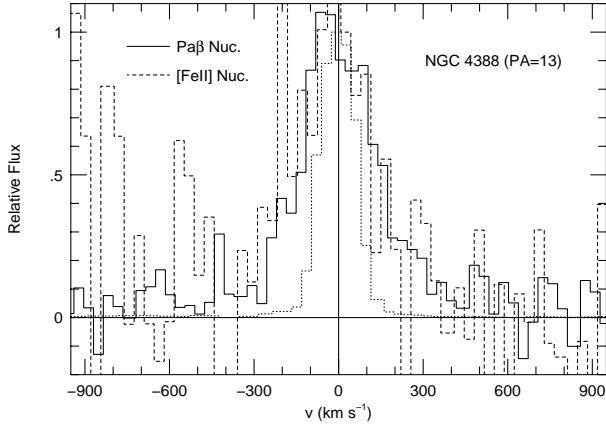


Figure 9. Comparison of the HR Pa β (full line) and [Fe II] 1.26 μ m (dashed line) nuclear spectral profiles of NGC 4388 along PA=13°. The dotted line is the instrumental profile, from the HeAr comparison lamp spectrum.

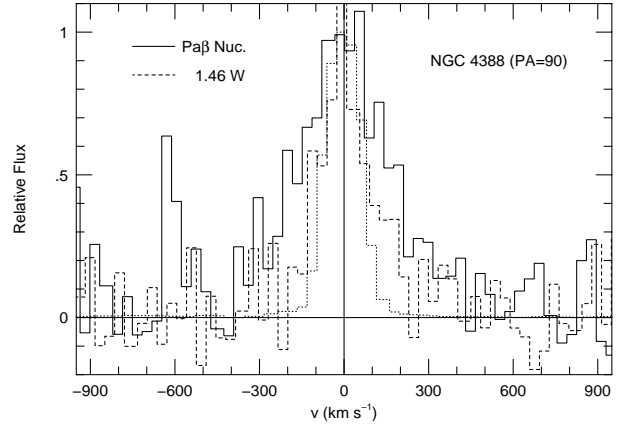


Figure 10. Comparison of the HR Pa β spectral profiles of NGC 4388 along PA=90°: nucleus (full line), and 1.46 W (dashed line). The dotted line is the instrumental profile, from the HeAr comparison lamp spectrum.

FWHM of $\sim 378 \text{ km s}^{-1}$. At 1.5 W of the nucleus the line is essentially unresolved (Fig. 10).

NGC 5643: The XD spectrum (Fig. 1c, bottom) was obtained along the axis of the optical ionization cone, and shows [S III], He I 1.083 μ m, Pa β , and the tip of the Pa α emission line. Only the Pa β profile is marginally resolved spatially in the central regions, but both this line and [S III] λ 9532 show a second emission feature $\sim 3''$ E of the nucleus, which may be associated with the filamentary extended emission seen in optical images (Schmitt, Storchi-Bergmann & Baldwin 1994; Simpson et al. 1997). In the central 2'', we measured [S III] λ 9532/(He I+Pa γ), [S III] λ 9532/Pa β , and (He I+Pa γ)/Pa β ratios of 1.34 ± 0.62 , 6.98 ± 1.03 , and 5.18 ± 0.71 , respectively.

NGC 5728: Two spectra (Fig. 1d) were obtained with the XD grating, at PA = 110°, the optical ionization cone direction, and perpendicular to it (PA = 20°). The S/N ratio is low, and only [S III] λ 9532, and He I+Pa γ are detected. The spatial profiles, shown in Figure 11, are resolved along both directions, although more extended at PA = 110° as expected from the optical images of Wilson et al. (1993). However, while He I+Pa γ is almost symmetric, the [S III] λ 9532 emission is stronger to the NW, the opposite direction of the optical cone. The [S III] λ 9532/(He I+Pa γ) ratio in the inner 4'' is 2.19 ± 0.85 along the cone, and 1.63 ± 0.94 perpendicular to it.

NGC 7582: This galaxy was observed with the slit at PA = 203°, which is within the optical ionization cone which has axis in PA $\approx 250^\circ$) (Storchi-Bergmann & Bonatto 1991). The peaks of the emission line spatial profiles (Fig. 12, top panel), are offset from the peak of the nearby continua by 0.7 – 0.8 to the NE, the opposite direction to the ionization

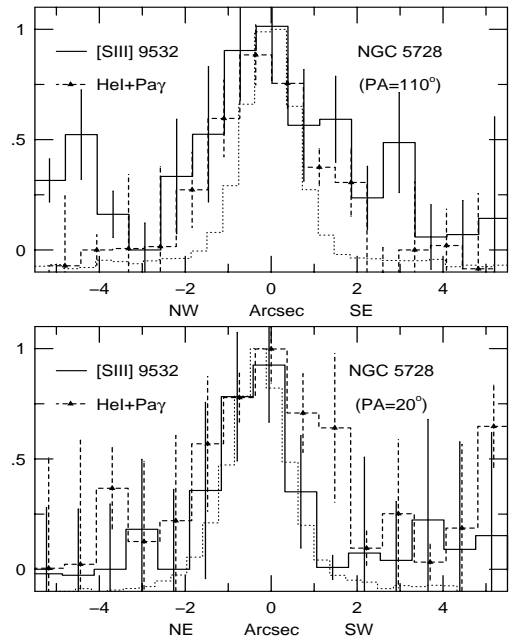


Figure 11. Spatial line profiles from the PA = 110° (top) and PA = 20° (bottom) XD spectra of NGC 5728. The error bars in the He I+Pa γ profile have been omitted for clarity and are of similar amplitude to those in the [S III] λ 9532 distribution. The dotted line is the stellar profile.

cone. All emission lines, with the possible exception of $\text{Pa}\beta$ are extended towards the cone. The $[\text{Fe II}] 1.64\mu\text{m}$ emission presents a double peaked structure, with an unresolved core plus a secondary bump reaching $\sim 2''.5$ SW. The $[\text{S III}] \lambda 9532$ profile is marginally extended to the NE. The double-peaked structure of the $[\text{Fe II}] 1.64\mu\text{m}$ emission is evident in the line-ratio distribution: to the NE, the $[\text{Fe II}] 1.64\mu\text{m}/\text{Pa}\beta$ ratio (Fig. 12, middle) is essentially constant at 0.45 ± 0.08 , reflecting the similar light distribution of the two lines; to the SW, the ratio increases sharply to 4.4 at $1''.6$, and then falls back to ~ 0.3 at $2''.5$.

In the absence of significant reddening, and taking the intrinsic ratio between the $[\text{Fe II}] \lambda 1.64\mu\text{m}$ and $\lambda 1.26\mu\text{m}$ lines as 0.75, these values translate to a $[\text{Fe II}] 1.26\mu\text{m}/\text{Pa}\beta$ ratio between 0.6 and 6, similar to those found above for NGC 1386 or in Paper I for the extended high excitation gas in NGC 2110. Note that contrary to what was observed for NGC 2110, where the nuclear $[\text{Fe II}]/\text{Pa}\beta$ ratio was quite high (~ 7), the nucleus of NGC 7582 presents a much lower ratio than the extended emission, with only a small excess over the expected ratio for young starbursts. Towards the cone, however, the tenfold increase in the $[\text{Fe II}]/\text{Pa}\beta$ ratio suggests the presence of an additional source of ionization, either excitation by X-ray photons from the active nucleus, escaping preferably towards the cone (due to shadowing by the torus) or the interaction of the radio plasma with the ambient medium. The recent radio maps of Morganti et al. (1999) show that the 3.5 cm emission is indeed extended and spatially coincident with the inner regions of the extended $\text{H}\alpha$ and $[\text{O III}]$ emission (Storchi-Bergmann & Bonatto 1991).

If there is significant intervening reddening ($A_V \sim 13$ mag from the $[\text{Fe II}] 1.64\mu\text{m}/1.26\mu\text{m}$ integrated line ratio from Table 3; or $A_V \lesssim 8$ mag from the continuum colours, see Section 3.2), the above observed values would translate to an intrinsic ratio $[\text{Fe II}] 1.26\mu\text{m}/\text{Pa}\beta \gtrsim 1$ in the cone region, still requiring an additional source of ionization other than young starbursts. A corresponding increase towards the SW is not observed in the $[\text{S III}] \lambda 9532/\text{Pa}\beta$ ratio (Fig. 12, bottom), where we measured values of 0.61 ± 0.29 ($r < 3''$ NE) and 0.34 ± 0.13 ($r < 3''$ SW).

ESO 362-G18: Our XD spectrum of this Seyfert 1 galaxy (Fig. 1e, top) was obtained along $\text{PA} = 68^\circ$, which is perpendicular to the direction of the axis of the approximately cone-shaped high-excitation gas emission region (Mulchaey et al. 1996). The spectrum presents bright broad lines including $\text{He II} + \text{Pa}\delta$, $\text{He I} + \text{Pa}\gamma$, $\text{Pa}\beta$, and $\text{Pa}\alpha$, which is located close to the atmospheric absorption between the H and K bands and the flux must be regarded as a lower limit. The permitted lines spatial profiles (Fig. 13) are extended towards the SW, which can be identified with the emission structure seen in the optical $\text{H}\alpha + [\text{N II}]$ images of Mulchaey et al. (1996). The distribution of the $(\text{He I} + \text{Pa}\gamma)/\text{Pa}\beta$ line ratio is approximately symmetric, with a maximum of ~ 7.2 about $0''.5$ SW of the continuum peak, and decreasing to ~ 1.5 at $3''$ both sides. The behaviour of the $(\text{He II} + \text{Pa}\delta)/(\text{He I} + \text{Pa}\gamma)$ ratio is quite different, with an essentially constant value of 0.29 ± 0.16 in the $r < 2''$ region.

Mrk 509: This is a Sy 1 galaxy suggested by Phillips et al. (1983) as presenting a face-on outflow. The XD spectrum in Figure 1e (middle) was obtained along the N-S direction. The spatial profiles (Fig. 14, top) are slightly resolved, and more extended towards the South,

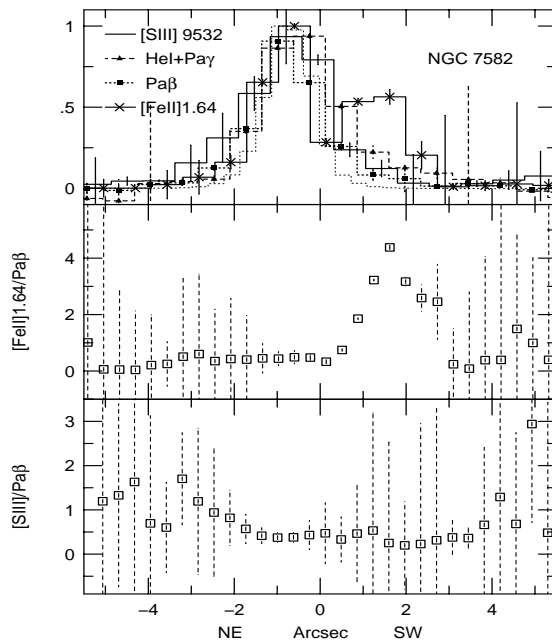


Figure 12. Spatial profiles and line ratios from the XD spectrum of NGC 7582. The dotted line is the stellar profile. Note that the origin of the spatial axis corresponds to the nearby *continuum* peak for each line.

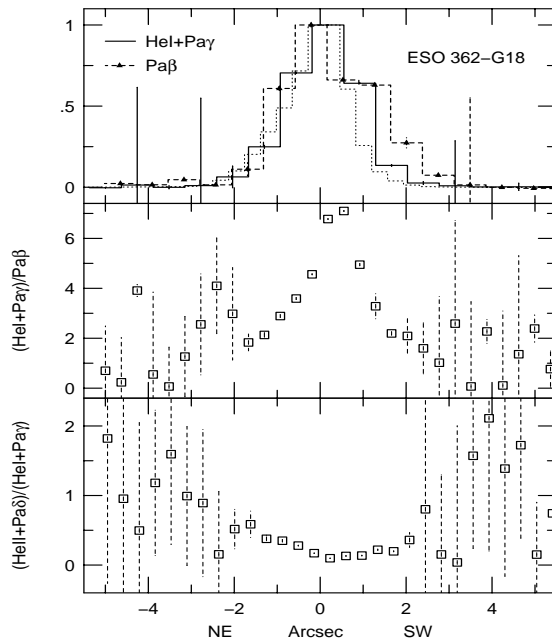


Figure 13. Same as Fig. 12 for ESO 362-G18.

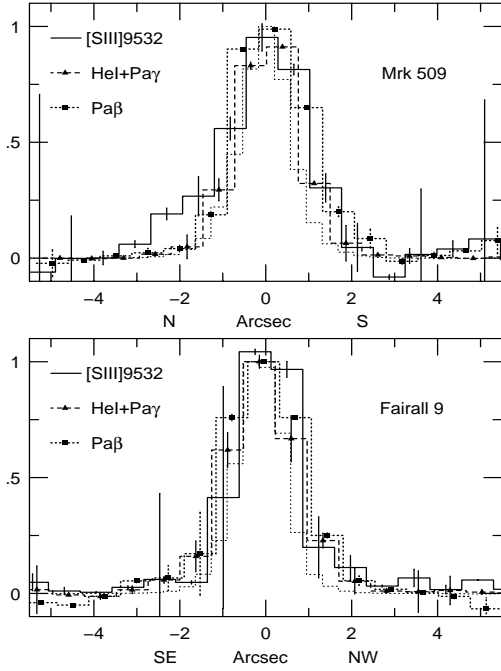


Figure 14. The spatial emission line profiles from the XD spectra of Mrk 509 (top) and Fairall 9 (bottom). The dotted line is the stellar profile.

with the exception of the [S III] $\lambda 9532$ line, which also shows extended emission up to $3''$ N of the nucleus. The line ratios in the inner $4 - 5''$ are dominated by the nuclear source, with $[S III] \lambda 9532 / Pa\beta = 0.42 \pm 0.13$, $[S III] \lambda 9532 / (He I + Pa\gamma) = 0.10 \pm 0.03$, $(He I + Pa\gamma) / Pa\beta = 3.50 \pm 0.52$, and $(He II + Pa\delta) / (He I + Pa\gamma) = 0.19 \pm 0.01$.

Fairall 9: The XD spectrum of this classical Sy1 nucleus is very similar to that of Mrk 509 (Fig. 1e). The brightest line is also He I + Pa γ and the spatial profiles (Fig. 14, bottom) are essentially unresolved, with $[S III] \lambda 9532 / Pa\beta$, $[S III] \lambda 9532 / (He I + Pa\gamma)$, $(He I + Pa\gamma) / Pa\beta$, and $(He II + Pa\delta) / (He I + Pa\gamma)$ in the inner $4 - 5''$ of 0.50 ± 0.08 , 0.10 ± 0.03 , 3.30 ± 0.33 , and 0.16 ± 0.01 , respectively.

NGC 1097: We obtained a LR spectrum in the J-band of this LINER nucleus in order to determine if the broad double-peaked profile observed in H α (Storchi-Bergmann, Baldwin & Wilson 1993) was also present in Pa β . The long-slit spectrum, however, shows Pa β emission only from an H II in the circumnuclear star-forming ring, $8''.7$ SW of the nucleus (Fig. 2a, top panel). This is a clear case of a very low luminosity, rather than dust obscured active nucleus.

IC 5063: Only a LR K-band spectrum (Fig. 2b, top) was obtained, under non-photometric conditions. The orientation of the slit was PA = 90° , which is close to that of the radio/optical/infrared structures in the inner few arcsec (Simpson, Ward & Kotilainen 1994; Morganti, Oosterloo & Tsvetanov 1998; Kulkarni et al. 1998), and both Br γ and H₂ $\nu=1-0$ S(1) lines were detected.

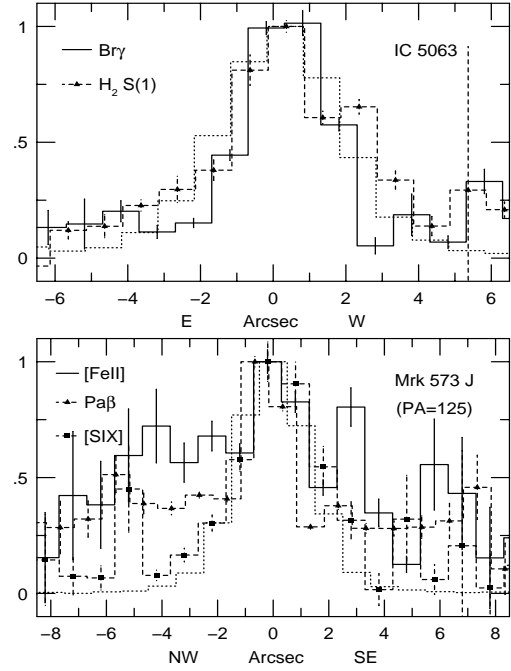


Figure 15. Spatial profiles from the LR spectra of IC 5063 (K-band, top) and Mrk 573 (J-band, bottom). The dotted line is a stellar profile.

The Br γ spatial distribution is unresolved, while the H₂ line appears to be only slightly resolved (Fig. 15, top). The H₂/Br γ ratio can be used to discriminate between the possible excitation mechanisms for H₂ emission: in star-forming regions, where the main heating agent is the UV photons, $H_2/Br\gamma < 1.0$ is expected, while additional H₂ emission excited by shocks or by X-rays from the active nucleus increases the observed values to up to 3 or more in Seyferts (Fischer et al. 1987; Moorwood & Oliva 1990; Kawara, Nishida & Gregory 1990; Veilleux et al. 1997). In our spectrum, we measured $H_2/Br\gamma = 1.22 \pm 0.20$ in the inner $5''$, which constitutes marginal evidence of a contribution from the active nucleus. The luminosity in the H₂ line can be used to estimate the mass of hot molecular hydrogen in the nuclear region. If the hot H₂ molecules are thermalized at T=2000 K, and assuming that the emission in all H₂ lines is 10 times that in the S(1) line (Scoville et al. 1982, Veilleux et al. 1997), the observed H₂ $\nu=1-0$ S(1) luminosity of $L(H_2) = 1.35 \times 10^{39}$ ergs s⁻¹ translates into a hot H₂ mass of about $450 M_\odot$.

The spectral profiles of the H₂ and Br γ lines are unresolved, except for the H₂ emission in the $1''.5$ NW spectrum (Fig. 16, top), which has an observed FWHM of ~ 630 km s⁻¹, corresponding to a intrinsic width of 484 ± 100 km s⁻¹.

Mrk 573: Two LR spectra were obtained for this galaxy. The J-band spectrum (Fig. 2b, middle) was taken along the radio continuum and optical emission-line axis at PA = 125° (Pogge & de Robertis 1995; Falcke, Wilson & Simpson

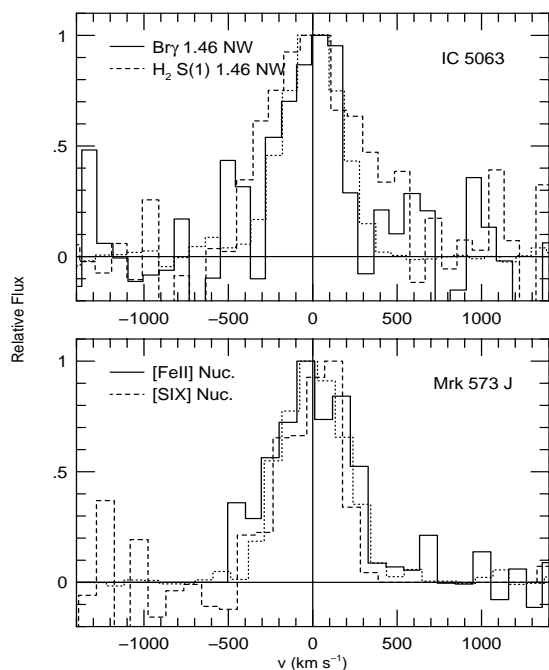


Figure 16. Top: comparison of the LR spectral line profiles of the K-band spectrum of IC 5063: $1''.46$ NW $\text{Br}\gamma$ (full line) and H_2 S(1) (dashed line). Bottom: J-band ($\text{PA}=125^\circ$) nuclear spectrum Mrk 573: $[\text{Fe II}]$ $1.26\mu\text{m}$ (full line) and $[\text{S IX}]$ (dashed line) profiles. The dotted lines in the top and bottom panels are, respectively, the $\text{Br}\gamma$ and $\text{Pa}\beta$ profiles of NGC 7009, which are taken as representative of the instrumental resolution.

1998), and presents $[\text{S IX}]$, $[\text{Fe II}]$ $1.26\mu\text{m}$, and $\text{Pa}\beta$ emission. Individual spectra, extracted in $0''.73$ increments (Fig. 17), as well as the spatial profiles (Fig. 15, bottom) clearly show that the $[\text{S IX}]$ distribution is unresolved, while $\text{Pa}\beta$ and $[\text{Fe II}]$ $1.26\mu\text{m}$ are extended. The $[\text{Fe II}]$ $1.26\mu\text{m}$ spatial profile presents a weak central peak with a flat extension towards the NW, reaching up to $\sim 8''$, while the SE side is less prominent, but equally extended. On the other hand, the $\text{Pa}\beta$ distribution is characterized by a well-defined, spatially unresolved, central core, and extended emission of almost equal intensity on both sides of the nucleus. The $[\text{Fe II}]$ $1.26\mu\text{m}/\text{Pa}\beta$ ratio has a mean value of 0.77 ± 0.14 in the inner $5''$.

A K band LR spectrum of Mrk 573 (Fig. 2b, bottom) was obtained at $\text{PA} = 35^\circ$, perpendicular to the direction of the radio jet. $\text{Br}\gamma$, possibly broad, and narrow H_2 $\nu=1-0$ S(1) were detected. Extracted spectra, in increments of $0''.73$, are shown in Figure 18.

In the J band spectra, along $\text{PA} = 125^\circ$, the spectral profile of $\text{Pa}\beta$ is unresolved up to $3''.3$ NW and SE. The $[\text{S IX}]$ line, detected only in the nuclear spectrum, is also unresolved, while $[\text{Fe II}]$ $1.26\mu\text{m}$ is marginally resolved spectrally in the nucleus but not outside (Fig. 16, bottom panel). In the K band, the H_2 nuclear spectral profile is too noisy to yield any information, while $\text{Br}\gamma$ is clearly resolved (Fig. 19), with an intrinsic width of $\sim 590 \text{ km s}^{-1}$, and some sugges-

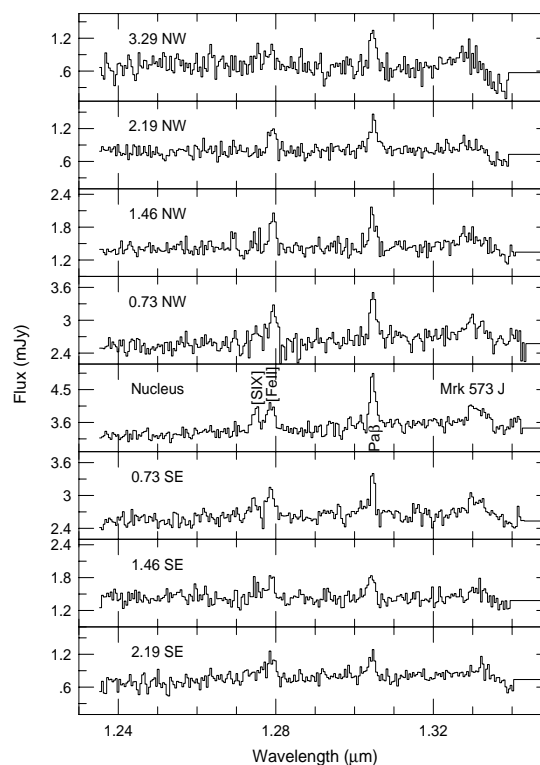


Figure 17. Individual J band spectra for Mrk 573. Bin size is $0''.73$ ($1''.46$ for the outermost position), centred at the distance from the nucleus indicated in the individual panels.

tion of a broad component ($\text{FWZI} \approx 1900 \text{ km s}^{-1}$), which contains about 70 percent of the total flux in the line, and is not observed in $\text{Pa}\beta$ ($\text{FWZI} \lesssim 1100 \text{ km s}^{-1}$). Taking the upper limit for the flux of a similar broad component in $\text{Pa}\beta$ as $\sim 5 \times 10^{-15} \text{ ergs cm}^{-2} \text{ s}^{-1}$ (calculated from the rms of the continuum around $\text{Pa}\beta$, and a FWHM of 1300 km s^{-1} obtained from Gaussian decomposition of the $\text{Br}\gamma$ profile), we have $\text{Br}\gamma/\text{Pa}\beta \gtrsim 0.6$, implying a reddening of $A_V \gtrsim 9$ mag in our line of sight to the broad line region in this galaxy.

Except for the presence of the broad base in $\text{Br}\gamma$, our results are in good agreement with those of Veilleux et al. (1997), which also found that $\text{Pa}\beta$ and H_2 $\nu=1-0$ S(1) were narrower than $[\text{Fe II}]$ $1.26\mu\text{m}$ or $\text{Br}\gamma$, with this last line presenting an intrinsic width of $\sim 550 \text{ km s}^{-1}$. Taking the narrow component of $\text{Br}\gamma$ as containing about one third of the observed line flux, the $\text{H}_2/\text{Br}\gamma$ ratio is ~ 1.2 , and would indicate some marginal evidence of H_2 excitation by X-rays from the active nucleus. Using the same assumptions as for IC 5063 the observed luminosity of H_2 $\nu=1-0$ S(1) in the inner $3''$ translates into a mass of hot H_2 of $\approx 300 M_\odot$.

3.2 Continuum

In this section, we present and analyse $(J-H)$ and $(H-K)$ colour profiles derived from our XD spectra. Previous studies of the central (less than 1 kpc) region of Seyfert galaxies have

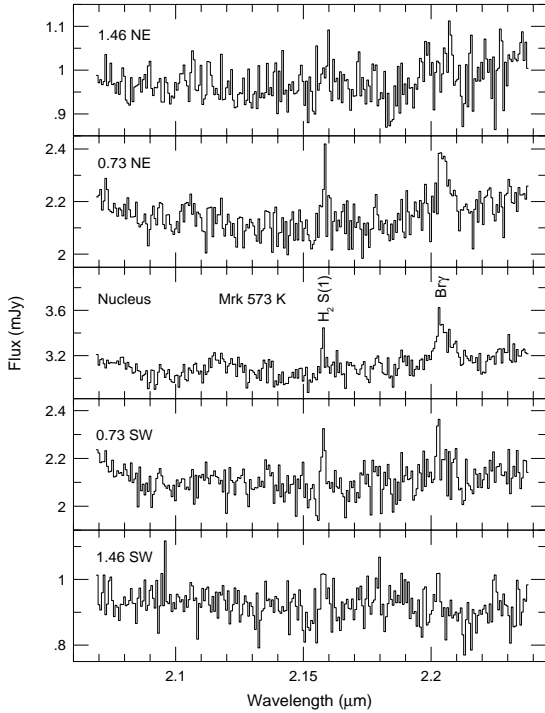


Figure 18. Same as Fig. 17, for the LR K band spectrum of Mrk 573.

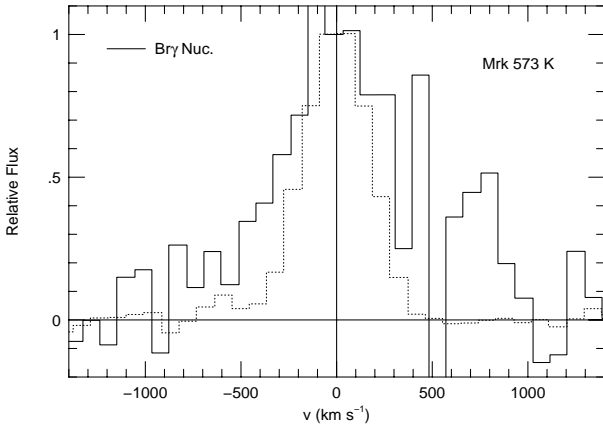


Figure 19. The nuclear Br γ LR spectral line profiles of Mrk 573 (K band, PA=35°). The dotted line is the Br γ profile of NGC 7009, which is taken as representative of the instrumental resolution.

shown that their near-IR colours are well explained either by a mixture of an evolved stellar population plus emission from hot (800 – 1200 K) dust, with varying foreground reddening (Alonso-Herrero, Ward & Kotilainen 1996, hereafter AH96), or by a model more closely associated to the dusty torus scenario, in which the starlight is not significantly reddened, while the nuclear continuum source is represented by hot dust ($T \approx 1200$ K) reddened by $A_V \approx 5 - 30$ mag (Alonso-Herrero et al. 1998, hereafter AH98). The off-nuclear colours show little evidence of hot dust emission, except for a few cases where the effect is attributed to the presence of massive stars acting as heating sources.

To obtain the colour profiles, the calibrated spectra were rebinned to 0.8 arcsec/pixel, then multiplied by the transmission curve of the corresponding filter, obtained from the CTIO web site[§], integrated along the wavelength direction and converted from flux to magnitudes. With an average seeing of $1 - 1''.5$, each profile is sampled by $1 - 2$ pixels.

Table 6 lists the nuclear ($r < 0''.8$) and ‘bulge’ ($0''.8 < r < 2''$) colours derived from the above profiles. These intervals correspond to linear scales of ~ 45 to 750 pc for the inner and outer radii in the Seyfert 2 galaxies in the sample. The errors correspond to the rms around the mean of the colour in the aperture, not the observational error. Figure 20 shows four representative colour profiles: some are very flat, as in NGC 1386, while others show redder ($H - K$) colour in the nuclear region or asymmetric profiles, as in NGC 3281 and NGC 7582, respectively. The colours in NGC 5253 are highly inhomogeneous, as might be expected from the clumpy nature of the distribution of the gas and presumably the reddening in this galaxy.

The data in Table 6 are in agreement with previous conclusions (AH96, AH98, Kotilainen et al. 1992, hereafter K92) that the nuclei of Seyferts tend to be redder than their bulges in one or both ($J - H$), ($H - K$) colours. Using the full profile, our data agrees with the $1''.5$ and $3''$ aperture photometry colours published in the literature within 0.1 – 0.2 mag for most objects, except NGC 4388, where our ($H - K$) colour is ~ 0.5 mag redder than the published values (AH96, AH98). We also find that for a few galaxies there is a 0.3 – 0.4 mag difference in the colours, most remarkably ($J - H$), of the ‘bulge’ regions at opposite sides of the nucleus.

The ($J - H$) versus ($H - K$) colour-colour diagrams of Figures 21a to 21f are based on the work of Alonso-Herrero et al. (1998). The shaded square to the left represents the colours of bulges of normal spiral galaxies (a late-type stellar population), while the one to the right represents the typical colours of quasars, corrected to zero redshift. The area bounded by dashed lines in the lower left corner of Figs. 21c and 21g corresponds to the region occupied by a young/intermediate age stellar population component with ages ranging from 10^6 to 10^8 years, calculated from the models of Leitherer & Heckman (1995). The arrow in the upper-left hand corner represents the effects of 2 mag of visual extinction. The ‘mixing curves’ represented by the dashed lines are the colours of the sum of a late-type stellar population and either a black-body component (assumed to be representative of hot dust emission) with temperatures $T =$

[§] We have used the curves of the filters in use with the CIRIM camera – j40, h44, k50, for J, H, and K, respectively

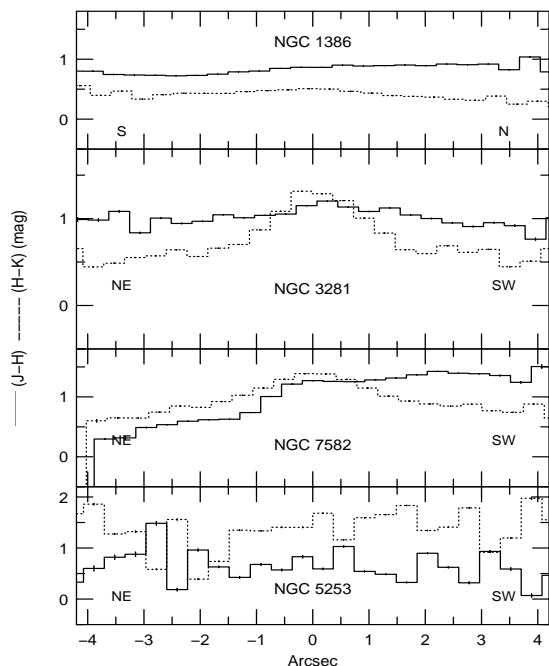


Figure 20. Four representative $(J-H)$ (full line) and $(H-K)$ (dotted line) colour profiles derived from the XD spectra of the sample galaxies. The orientation is the same as for the line profiles shown in section 3.1 and is also indicated in the individual panels.

600, 800, 1000, and 1200K, or a nebular component, corresponding to hydrogen and helium continuum and line emission. The dotted lines (diagonal slashes) are the loci of the colours for the given ratio of dust (nebular) to stellar luminosities in the K band. The results for each individual galaxy are described below.

NGC 5253: Fig. 21c – the data points are scattered over the bottom right of the diagram. Since the long slit spectrum indicates little or no continuum emission, the data can be understood as nebular emission plus spatially inhomogeneous reddening and/or dust emission. From the $\text{Br}\gamma/\text{Pa}\beta$ ratio, we found regions with $A_V \sim 8$ mag, which would be enough to shift the points from the nebular emission curve to the observed location at the middle of the diagram.

NGC 526A: Fig. 21b – the data points follow different paths in the cone (SE) and anti-cone (NW) direction, with the $(J-H)$ colour in the region $0''.8 - 1''.4$ SE about 0.3 mag redder than to the NW. This behaviour suggests difference in the underlying stellar population content between the two sides of the nucleus. As can be seen in Fig. 21, the loci of old (left grey square) and young-intermediate (area at bottom left limited by dashed lines) stellar populations are separated by ~ 0.8 mag in $(J-H)$, with very little difference in the corresponding $(H-K)$ colours. Reddening effects are also very likely present and cannot be discarded as contributing to the observed colours. In the central bin ($0''.8$), the colours suggest hot dust emission dominates the continuum.

NGC 1365: Fig. 21f – the colours behave somewhat similarly to NGC 526A, although with the nuclear colour cor-

responding to a smaller ratio of hot dust to starlight emission. The bluer $(J-H)$ colour towards the NW may result from contamination of the ‘normal’, old bulge population by younger stars in the ‘hot spots’ (see Storchi-Bergmann & Bonatto 1991; Morganti et al. 1999).

NGC 1386: Fig. 21b – Both colour profiles (Fig. 20) are essentially flat, with $(J-H)$ rising slightly towards the North (the optical cone direction) and $(H-K)$ showing only a hint of a redder colour in the nuclear region. In the colour-colour plot, the points concentrate near the pure bulge region, with little or no contribution from hot dust. The orientation of both the high excitation optical and radio emission (Storchi-Bergmann et al. 1996; Weaver et al. 1991), as well as the fact that NGC 1386 contains water vapour megamaser emission (Braatz, Wilson & Henkel 1996), suggest that the collimating structure is seen edge-on. Therefore, the hot dust in the inner regions may be obscured by colder dust further out in the disk, resulting in a small contribution from the nucleus to the near infrared continuum.

NGC 2110: Fig. 21h – The analysis of the J and K band continua presented in Paper I indicates the presence of a hot dust component in the inner ~ 150 pc, consistent with emission by a circumnuclear torus. The observed colour profiles confirm this finding: while the $(J-H)$ distribution is essentially flat across the nucleus, the $(H-K)$ colour increases by about 0.5 mag in the inner $2''$ relative to the external regions. In the colour-colour diagram, ignoring the foreground galactic reddening ($E(B-V)_G \sim 0.36$; Burstein & Heiles 1982), the points trace a continuous path from pure bulge colours to a combination of bulge and a ~ 1200 K black-body component at the nucleus.

NGC 3281: Fig. 21g – The colour profiles (Fig. 20) present a similar behaviour to that observed in NGC 2110, with the variation in $(H-K)$ colour being even more pronounced, with a 0.7 mag decrease from the nucleus to the bulge. This would indicate a higher fraction of hot dust emission in the nuclear region than in the NGC 2110 case, but of a somewhat lower temperature (~ 1000 K).

NGC 4388: Fig. 21e – The $(H-K)$ colour is redder at the nucleus than in the bulge at $\text{PA} = 13^\circ$, similar to what is observed in NGC 2110 and NGC 3281. The effect is much less apparent at $\text{PA} = 90^\circ$, which can be understood if, as mentioned in Section 3.1, we missed the nucleus on this observation. Both PA ’s occupy the same region in the colour diagram, and the data points for the whole inner $5-6''$ (~ 1 kpc) are shifted towards redder $(H-K)$ colours when compared with other published values (K92, AH98).

NGC 5643: Fig. 21d – The colour profiles are flat across the nucleus. In the colour diagram, the points cluster near the bulge colours, with a small contribution from dust emission or a foreground reddening of $A_V \sim 1.5 - 2$ mag. Again, this could be a case of a torus either too cold to emit in the near infrared or with inner regions obscured from our line of sight by the outer ones.

NGC 5728: Fig. 21e – For $\text{PA} = 110^\circ$, both colour profiles are rather flat. In the colour-colour plot, the data points cluster close to normal bulge colours, similar to what is observed for NGC 5643. Along the perpendicular direction ($\text{PA} = 20^\circ$), $(J-H)$ is somewhat redder and $(H-K)$ bluer towards the SW than to the NE.

NGC 7582: Fig. 21h – The $(H-K)$ profile (Fig. 20) exhibits the same behaviour as observed in NGC 2110 and

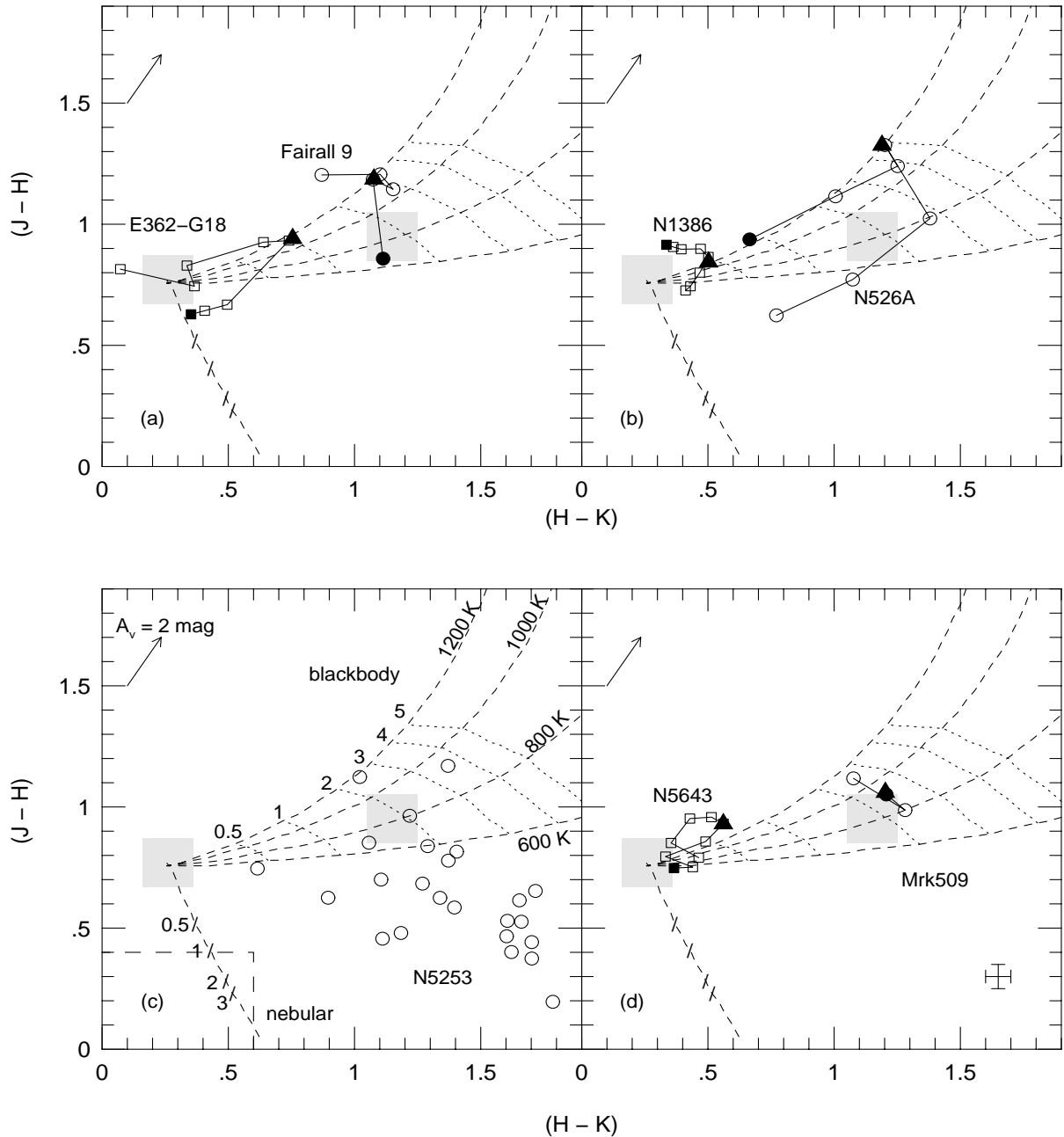


Figure 21. $(J-H)$ vs $(H-K)$ colour-colour diagrams (adapted from Alonso-Herrero et al 1998). See text for an explanation of the mixing curves and other symbols. For each object, the filled triangle represents the nucleus, while the filled circle/square is the most distant point from the nucleus on the cone (positive) side of the profile. The bin size is $0''.8$ and the spatial interval (in arcsec) represented is as follows: (a) ESO 362-G18 (-3.4 NE, 3 SW) and Fairall 9 (-2.6 SE, 1.4 NW); (b) NGC 1386 (-3.4 S, 3 N) and NGC 526A (-2.6 NW, 3 SE); (c) NGC 5253 (-4 NE, 4 SW; bin $0''.4$); (d) NGC 5643 (-3.4 W, 3.8 E) and Mrk 509 (-1.8 N, 1.4 S).

Table 6. Nuclear and bulge colours

Object	Nucleus ($R < 0''.8$)			Bulge ($0''.8 < R < 2''$)				
	$(J-H)$	$(H-K)$		$(J-H)$	$(H-K)$	$(J-H)$	$(H-K)$	
NGC 526A	1.27±0.03	1.24±0.04	NW	0.88±0.07	1.25±0.10	SE	1.12±0.03	0.99±0.13
NGC 1365	1.07±0.03	0.97±0.03	NW	0.78±0.03	0.94±0.08	SE	1.05±0.03	0.57±0.05
NGC 1386	0.87±0.01	0.49±0.01	S	0.77±0.02	0.45±0.01	N	0.89±0.01	0.40±0.02
NGC 2110	1.01±0.01	0.94±0.02	SE	1.02±0.02	0.66±0.07	NW	1.01±0.04	0.68±0.05
NGC 3281	1.13±0.03	1.21±0.06	NE	1.02±0.01	0.72±0.06	SW	1.08±0.02	0.79±0.10
NGC 4388 (13)	0.89±0.01	1.42±0.03	N	0.88±0.02	1.19±0.04	S	1.02±0.07	1.16±0.04
NGC 4388 (90)	1.03±0.02	1.51±0.02	W	0.85±0.05	1.35±0.04	E	1.01±0.01	1.28±0.08
NGC 5643	0.93±0.01	0.54±0.01	W	0.94±0.02	0.41±0.03	E	0.82±0.02	0.42±0.05
NGC 5728 (110)	0.94±0.02	0.45±0.03	NW	0.84±0.01	0.53±0.02	SE	0.94±0.01	0.32±0.01
NGC 5728 (20)	1.04±0.03	0.39±0.03	NE	0.87±0.05	0.51±0.01	SW	1.12±0.01	0.11±0.05
NGC 7582	1.21±0.04	1.33±0.03	NE	0.70±0.06	0.99±0.07	SW	1.31±0.03	1.02±0.06
ESO 362-G18	0.90±0.04	0.69±0.04	NE	0.84±0.03	0.38±0.05	SW	0.65±0.01	0.44±0.03
Fairall 9	1.14±0.03	1.11±0.02	SE	1.19±0.02	1.08±0.07	NW	0.77±0.05	1.06±0.03
Mrk 509	0.98±0.05	1.24±0.02	N	1.11±0.07	1.05±0.13	S	0.59±0.06	1.07±0.07

NGC 3281, with the nuclear colour ~ 0.5 mag redder than the bulge. The $(J-H)$ profile, however, rises steadily to the SW, with a 0.8 mag increase from $3''$ NE to $3''$ SW (the cone side). In the colour-colour diagram, the nucleus corresponds to a dominant contribution from ~ 1000 K black-body emission. The data points starting at $3''$ NE can be interpreted as a reddened evolving starburst, with increasing reddening towards the nucleus (up to $A_V \sim 8$ mag). The colours observed on the SW (cone) side of the nucleus are suggestive of a reddened, old stellar population.

ESO 362-G18: Fig. 21a – The data points start with bulge colours at $3''$ NE, run along a line of increasing contribution from hot dust, up to a maximum of equal contributions from both sources at the nucleus, and then return with $(J-H)$ colours ~ 0.2 mag bluer towards the SW. This effect can again be explained by a different underlying stellar population: an evolving starburst is bluer in $(J-H)$ but occupies almost the same region in $(H-K)$ as the typical late-type, bulge population.

Mrk 509 and *Fairall 9*: Fig. 21d and 21a – the PSF of the nucleus dominates the inner $4''$ due to the brightness of the central source. Since the sources are unresolved, the data points cluster around the colours characteristic of quasars, as expected for these type 1 Seyfert galaxies.

4 SUMMARY AND CONCLUSIONS

We obtained near-infrared, long-slit spectra for a sample of 12 Seyfert 2s, 3 Seyfert 1s, and the starburst galaxy NGC 5253, using as the main selection criterion the presence of extended high-excitation emission observed in optical images. From our analysis of the spatial, and spectral emission-line profiles, and of the continuum $(J-H)$ and $(H-K)$ colours, we conclude that:

- consistent with the selection criteria, 9 of the 12 objects with extended optical emission lines also present extended emission lines in the near-IR along the position angle of the optical ionization cones or radio emission. In three cases, however, we found that the near-IR emission lines were also extended along PAs oriented perpendicular to the

optical/radio emission axis. The clearest case where high-excitation near-IR line emission traces the optical ionization structure is NGC 7582, where the emission lines in the inner few arcsec are extended along the direction of the optical cone. Interestingly, the maxima of the emission-line distributions in this galaxy are consistently offset from the peak of the continuum emission by $\sim 0''.8$ in the direction opposite to the optical cone. Besides the central peak, the spatial profile of the [Fe II] $1.64\mu\text{m}$ line in NGC 7582 presents a secondary structure between $0''.5$ and $2''.5$ SW, with the [Fe II] $1.64\mu\text{m}/\text{Pa}\beta$ ratio increasing from ≈ 0.5 at the position of the continuum peak to 4.4 at $1''.6$ SW, indicating a different ionization mechanism for the [Fe II] line in this region. A similar result was found for NGC 1386, for which the [Fe II] $1.26\mu\text{m}/\text{Pa}\beta$ ratio rises from ≈ 2 to 6 between the nucleus and the optical extended emission-line region at $2''$ N. These high values and the presence of radio emission and/or a high velocity nuclear outflow spatially coincident with the optical ENLR suggest that shocks may play a role as an excitation mechanism for the off-nuclear [Fe II] line in both galaxies.

- the low resolution (XD) spectra are not sufficiently sensitive to detect the expected H_2 emission from the torus. However, in the few cases for which we have a high resolution K band spectra (Mrk 573, IC 5063, NGC 2110), the H_2 S(1) $\lambda 2.12\mu\text{m}$ was clearly detected.

- broad components have been observed in the permitted emission lines of the Seyfert 1 galaxies, in nuclear $\text{Pa}\beta$ in NGC 1365, and very likely in $\text{Br}\gamma$ in Mrk 573. In NGC 1365 the flux of the broad (FWHM $\approx 1500 \text{ km s}^{-1}$) component of $\text{Pa}\beta$ was used to estimate a reddening of $A_V \sim 8$ mag towards the BLR. A lower limit of ~ 9 mag was obtained for A_V towards the BLR of Mrk 573. In NGC 4388 and Mrk 573 the [S IX] $\lambda 1.262\mu\text{m}$ emission line was detected, and found to be spatially unresolved in both objects. With an ionization potential of 0.328 keV, the detection of this species is an indirect evidence of significant soft X-rays continuum flux in these galaxies. In NGC 5253, the $\text{Br}\gamma/\text{Pa}\beta$ ratio was used to map strong reddening variations, from $A_V \sim 0$ to 6 mag within the central $8''$.

- spatial $(J-H)$ and $(H-K)$ colour profiles were derived from our spectra. For most Seyfert 2s, the nuclear colours are

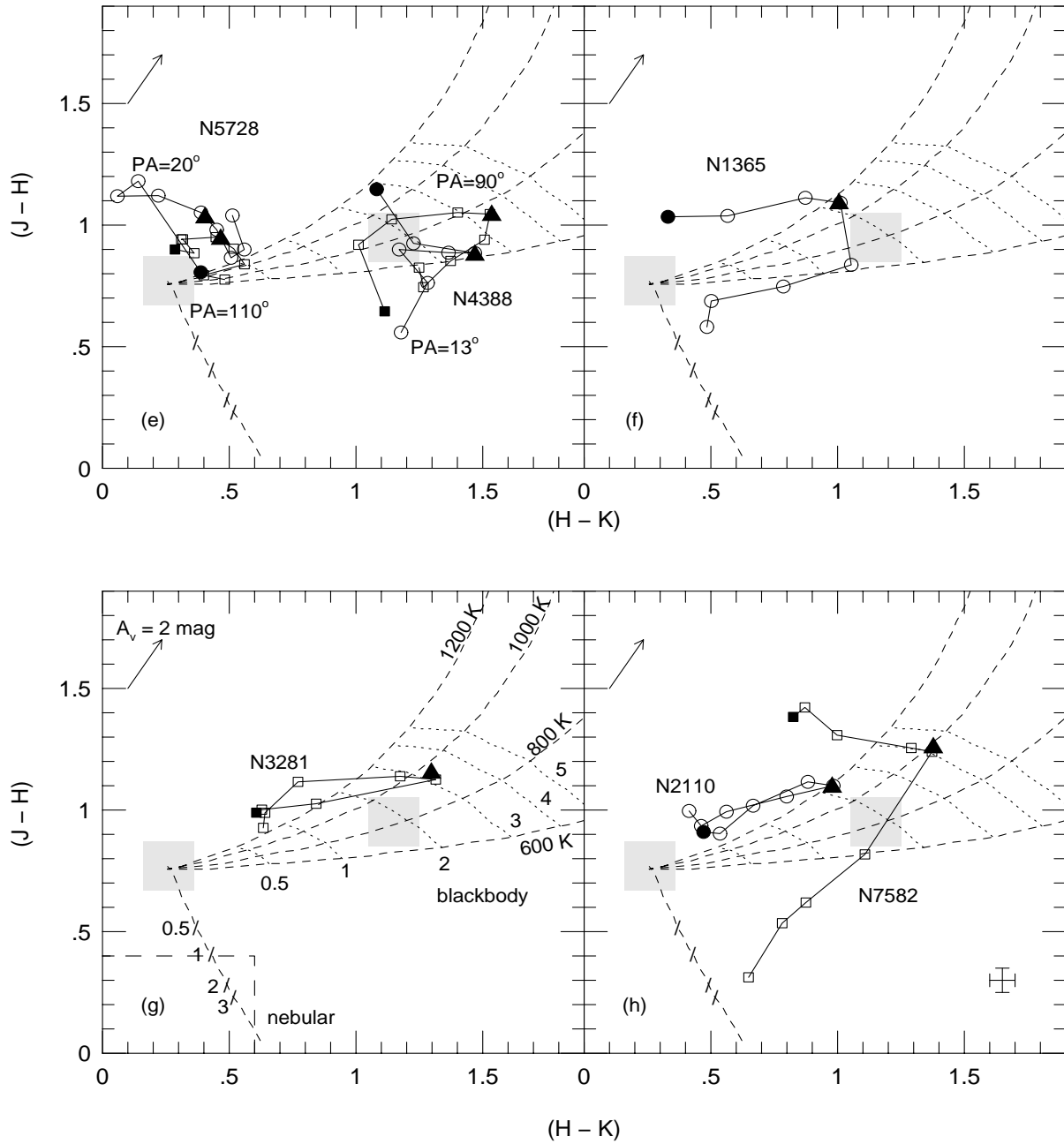


Figure 21 – *continued* (e) NGC 5728 (circles) PA=20° (-3.4 NE,3.8 SW), (squares) PA=110° (-3.4 NW,3.8 SE) and NGC 4388 (circles) PA=13° (-3.4 NE,2 SW), (squares) PA=90° (-3.4 W,3.8 E); (f) NGC 1365 (-2.8 NW,3.8 SE); (g) NGC 3281 (-3.4 NE,3 SW); (h) NGC 2110 (-3.4 SE,3.8 NW) and NGC 7582 (-3.4 NE,3.8 SW).

redder than the extranuclear values, with the nuclear continuum being dominated by hot ($T \sim 1000$ K) dust emission in NGC 1365, NGC 2110, NGC 3281, NGC 7582, and ESO 362-G18. In NGC 1386, NGC 5643, and NGC 5728, the nuclear colours are consistent with a continuum dominated by the emission from the underlying stellar population plus a smaller contribution from dust and/or foreground reddening effects. The Seyfert 1 nuclei, Mrk 509 and Fairall 9, have colours similar to quasars, as expected.

- the galaxies NGC 526A, NGC 1365, NGC 7582, and ESO 362-G18 show a clear difference between the ($J-H$) colours on each side of the nucleus. Since late-type (bulge) and young/intermediate stellar populations differ mostly in their ($J-H$) colour, ($H-K$) being approximately the same, we explain this effect by differences in the underlying stellar population, very likely coupled with reddening. The observed colour differences could indicate the presence of a younger/intermediate age component, associated, for example, with the star-forming rings known to exist in some of the observed galaxies, and which could provide a larger contribution to the near-IR continuum on one side of the nucleus relative to the other.

ACKNOWLEDGEMENTS

This work has made use of NASA's Astrophysics Data System Abstract Service (ADS), and of the NASA/IPAC Extragalactic Database (NED) which is operated by the Jet Propulsion Laboratory, California Institute of Technology, under contract with the National Aeronautics and Space Administration. Research partially supported by the Brazilian Agencies FAPERGS and CNPq.

REFERENCES

- Alonso-Herrero A., Ward M. J., Kotilainen J. K. 1996, MNRAS, 278, 902. (AH96)
- Alonso-Herrero A., Rieke M. J., Rieke G. H., Ruiz M. 1997, ApJ, 482, 747.
- Alonso-Herrero A., Simpson C., Ward M. J., Wilson A. S. 1998, ApJ, 495, 196. (AH98)
- Antonucci R. R. J. 1993, ARA&A, 31, 473.
- Braatz J. A., Wilson A. S., Henkel C. 1996, ApJS, 106, 51.
- Burstein D., Heiles C. 1982, AJ, 87, 1165.
- Blietz M., Cameron M., Drapatz S., Genzel R., Krabbe A., van der Werf P., Sternberg A., Ward M. 1994, ApJ, 421, 92.
- Calzetti D., Meurer G. R., Bohlin R. C., Garnett D. R., Kinney A. L., Leitherer C., Storchi-Bergmann T. 1997, AJ, 114, 1834.
- Colina L. 1993, ApJ, 411, 565.
- Falcke H., Wilson A. S., Simpson C. 1998, ApJ, 502, 199.
- Fischer J., Smith H. A., Geballe T. R., Simon M., Storey J. W. V. 1987, ApJ, 320, 667.
- Forbes D. A., Ward M. J. 1993, ApJ, 416, 150.
- Giannuzzo E. M., Stirpe G. M. 1996, A&A, 314, 419.
- Glass I. S., Moorwood A. F. M. 1985, MNRAS, 214, 429.
- Kawara K., Nishida M., Gregory B. 1990, ApJ, 352, 433.
- Kotilainen J. K., Ward M. J., Boisson C., DePoy D. L., Bryant L. R., Smith M. G. 1992, MNRAS, 256, 149.
- Kristen H., Jörsäter S., Lindblad P. O., Boksenberg A. 1997, A&A, 328, 483.
- Krolik J. H., Begelman M. C. 1988, ApJ, 329, 702.
- Kulkarni V. P. et al. 1998, ApJ, 492, L121.
- Leitherer C., Heckman T. M. 1995, ApJS, 96, 9.
- Lumsley S. L., Puxley P. J. 1996, MNRAS, 281, 493.
- Marco O., Alloin D., Beuzit J. L. 1997, A&A, 320, 399.
- Miller J. S., Goodrich R. W. 1990, ApJ, 378, 47.
- Moorwood A. F. M., Oliva E. 1990, A&A, 239, 78.
- Moorwood A. F. M., van der Werf P. P., Kotilainen J. K., Marconi A., Oliva E. 1996, A&A, 308, 1.
- Morganti R., Oosterloo T., Tsvetanov Z. 1998, AJ, 115, 915.
- Morganti R., Tsvetanov Z. I., Gallimore J., Allen M. G. 1999, A&AS, 137, 457.
- Morris S., Ward M., Whittle M., Wilson A. S., Taylor K. 1985, MNRAS, 216, 193.
- Mulchaey J. S., Wilson A. S., Tsvetanov Z. I. 1996, ApJS, 102, 309.
- Nagar N. M., Wilson A. S., Mulchaey, J. S., Gallimore J. 1999, ApJS, 120, 209.
- Osterbrock D. E. 1989 Astrophysics of Gaseous Nebulae and Active Galactic Nuclei, University Science Books, Mill Valley, California.
- Phillips M. M., Baldwin J. A., Atwood B., Carswell R. F. 1983, ApJ, 274, 558.
- Pier E. A., Krolik J. H. 1993, ApJ, 418, 673.
- Pogge R. W. 1989, ApJ, 345, 730.
- Pogge R. W., de Robertis M. M. 1995, ApJ, 451, 585.
- Schmitt H. R., Storchi-Bergmann T., Baldwin J. A. 1994, ApJ, 423, 237.
- Schmitt H. R., Storchi-Bergmann T., Cid Fernandes R. 1999, MNRAS, 303, 173.
- Scoville N. Z., Hall D. N. B., Ridgway S. T., Kleinmann S. G. 1982, ApJ, 253, 136.
- Simpson C., Ward M., Kotilainen J. 1994, MNRAS, 271, 250.
- Simpson C., Forbes D. A., Baker A. C., Ward M. J. 1996a, MNRAS, 283, 777.
- Simpson C., Mulchaey J. S., Wilson A. S., Ward M. J., Alonso-Herrero A. 1996b, ApJ, 457, L19.
- Simpson C., Wilson A. S., Bower G., Heckman T. M., Krolik J. H., Miley G. K. 1997, ApJ, 474, 121.
- Stevens I. R., Forbes D. A., Norris R. P. 1999, MNRAS, 306, 479.
- Storchi-Bergmann T., Bonatto C. J. 1991, MNRAS, 250, 138.
- Storchi-Bergmann T., Baldwin J. A., Wilson A. S. 1993, ApJ, 410, L11.
- Storchi-Bergmann T., Rodriguez-Ardila A., Schmitt H. R., Wilson A. S., Baldwin J. A. 1996, ApJ, 472, 83.
- Storchi-Bergmann T., Winge C., Ward M. J., Wilson A. S. 1999, MNRAS, 304, 35. (Paper I)
- Stone J. L. Jr., Wilson A. S., Ward M. J. 1988, ApJ, 330, 105.
- Tran H. D. 1995, ApJ, 440, 597.
- Ulvestad J. S., Wilson A. S. 1984, ApJ, 285, 439.
- Vanzi L., Alonso-Herrero A., Rieke G. H. 1998, ApJ, 504, 93.
- Veilleux S., Goodrich R. W., Hill G. J. 1997, ApJ, 477, 631.
- Veilleux S., Bland-Hawthorn J., Cecil G., Tully R. B., Miller S. T. 1999, ApJ, 520, 111.
- Véron P., Lindblad P. O., Zuiderwijk E. J., Adam G., Véron M. P. 1980, A&A, 87, 245.
- Weaver K. A., Wilson A. S., Baldwin J. A. 1991, ApJ, 366, 50.
- Wilson A. S., Baldwin, J. A., Ulvestad, J. S. 1985, ApJ, 291, 627.
- Wilson A. S., Braatz J. A., Heckman T. M., Krolik J. H., Miley G. K. 1993, ApJ, 419, L61.
- Wilson A. S., Tsvetanov Z. I. 1994, AJ, 107, 1227.

This paper has been produced using the Royal Astronomical Society/Blackwell Science L^AT_EX style file.